INDIRECT MEASUREMENT OF COSMIC-RAY PROTON SPECTRUM USING EARTH'S γ-RAY DATA FROM *FERMI* LARGE AREA TELESCOPE

PATOMPORN PAYOUNGKHAMDEE

A THESIS SUBMITTED IN PARTIAL FULFILLMENT
OF THE REQUIREMENTS FOR
THE DEGREE OF MASTER OF SCIENCE (PHYSICS)
FACULTY OF GRADUATE STUDIES
MAHIDOL UNIVERSITY
2021

Thesis
entitled

.....
Mr. Patomporn Payoungkhamdee
Candidate

.....
Asst. Prof. Warit Mitthumsiri,
Ph.D. (Physics)
Major advisor

.....
Prof. David Ruffolo,
Ph.D. (Physics)
Co-advisor

.....
Prof. Patcharee Lertrit,
M.D., Ph.D. (Biochemistry)
Dean
Faculty of Graduate Studies
Mahidol University

.....
Assoc. Prof. Kittiwit Matan,
Ph.D. (Physics)
Program Director
Master of Science Program in Physics
(International Program)
Faculty of Science
Mahidol University

Thesis
entitled

was submitted to the Faculty of Graduate Studies, Mahidol University
for the degree of Master of Science (Physics)
on
June 14, 2021

.....
Mr. Patomporn Payoungkhamdee
Candidate

.....
Asst. Prof. Waraporn Nuntiyakul,
Ph.D. (Physics)
Chair

.....
Asst. Prof. Warit Mitthumsiri,
Ph.D. (Physics)
Member

.....
Prof. David Ruffolo,
Ph.D. (Physics)
Member

.....
Prof. Patcharee Lertrit,
M.D., Ph.D. (Biochemistry)
Dean
Faculty of Graduate Studies
Mahidol University

.....
Assoc. Prof. Palangpon Kongsaree,
Ph.D. (Organic Chemistry)
Dean
Faculty of Science
Mahidol University

ACKNOWLEDGEMENTS

Throughout the working of this research project, I have received invaluable support and assistance. I would like to express my deepest appreciation to my supervisor, Asst. Dr. Warit Mitthunsiri, who sharpen my thinking, introduces me to the methodology as well as read my numerous revision. I would like to extend my sincere thanks to Prof. David Ruffolo, my co-advisor who leads the space physics laboratory, for insightful suggestions.

The completion of my dissertation would not have been smooth without the support and practical suggestions of Dr. Suttiwat Madlee, who assists me how to write the program and preparing the raw data for colleagues. I am also grateful to Asst. Dr. Waraporn Nuntiyakul, one of the the committee who gave me very beneficial advice. I also had the great pleasure of working with the members of space physics laboratory for academic guidance and the warm working environment. Many thanks to Dr. Francesca Spada and the group of people who working with *Fermi* Telescope at University of Pisa for the discussion in the analysis methodology during my internship in the junior year.

Last but not least, I gratefully acknowledge the academic discussion during my master's study with my friends. I would like to recognize the effort that I received from physics department, Mahidol University for both hardware and paperwork assistance. Special thanks to Development and Promotion of Science and Technology Talents Project (DPST) for any financial support Finally, I would like to thanks to my parents who endured this long process with me, always offering support and love.

Patomporn Payoungkhamdee

INDIRECT MEASUREMENT OF COSMIC-RAY PROTON SPECTRUM USING EARTH'S γ-RAY DATA FROM *FERMI* LARGE AREA TELESCOPE.

PATOMPORN PAYOUNGKHAMDEE 6138171 SCPY/M

M.Sc. (PHYSICS)

THESIS ADVISORY COMMITTEE: WARIT MITTHUMSIRI, Ph.D. (PHYSICS), DAVID RUFFOLO, Ph.D. (PHYSICS)

ABSTRACT

Cosmic rays (CRs) are high-energy particles, mostly protons, propagating in space. The rigidity (momentum per charge) spectrum of CRs is well described by a power law for which the spectral index is approximately 2.8 around 30 - 1000 GV. Recent measurements by PAMELA and AMS-02 indicate an abrupt change of the CR proton spectral index at about 340 GV. When CRs interact with the Earth's upper atmosphere, γ rays can be produced and detected by space-based detectors. Here we use the Earth's γ-ray data collected by the *Fermi* Large Area Telescope along with a proton-air interaction model to indirectly determine the CR proton spectral index and compare against observations by other instruments.

KEY WORDS: COSMIC RAYS / EARTH'S GAMMA RAYS

71 pages

CONTENTS

CONTENTS (cont.)

LIST OF TABLES

LIST OF FIGURES

CHAPTER I
INTRODUCTION

1.1 Overview

Space is full of fascinating phenomena and the questions, from why stars are bright to more advanced questions such as the nature of dark matter. Human curiosity has brought us so far that now we can observe the sky with more sophisticated techniques. However, the research to gather new knowledge by studying the space is endless. The answer to one question sometimes generates another mystery. Research in physical science also helps to create new technology because of the need to overcome challenging limitations of the instruments or techniques.

The frontier of astrophysical research is continually expanding over time because the exploration of one thing does open the new door to another dark room which has been waiting for human to shine a light to explore. There are various branches in astrophysics from theoretical foundation, simulation and experimental physics which all complement of them trying to push the frontier of human knowledge. To study high energy particle accelerators in the universe, the possibility of direct probing of multiple Galactic sources which produce high-energy particles, or cosmic rays (CRs), is nearly impossible in terms of current technology and resources required. Nevertheless, the technology of observing the particles arriving the Earth is more plausible for scientists.

CRs can be observed with two types of detectors: ground-based and spaced-based. Analyzing and studying CR data allows us to interpret the properties of their sources and cosmic environment.

The spectrum of CRs follows a power law with different spectral indices depending on the rigidity (momentum per charge) range of particles. There are multiple types of CR sources in space including unknown sources. Consequently,

changing of the spectral index from one rigidity to another rigidity will find the discontinuity if there is the translation from one source type to another source from the superposition of multiple spectrums.

Fermi-LAT has been launched to orbit around the Earth and monitor the γ-ray sky. Interestingly, the brightest γ-ray source in the sky for the LAT is the Earth's limb due to its proximity. At above 1 GeV, the Earth's γ-ray emission from CRs interacting with the upper atmosphere appears as a bright ring (Abdo et al. 2009).

Before 2010, there were some hints of the abrupt change in the CR spectral index at 300 GV in rigidity by some experiments (Adriani et al. 2011; Seo et al. 2004; Isbert et al. 2002; Haino et al. 2004), though the conclusion was from the combination of data from different experiments which is prone to the systematic uncertainty. In 2014, *Fermi*-LAT attempted to measure this spectral feature indirectly using the Earth's γ-ray emission data from 5 years of observations (Ackermann et al. 2014). The inferred spectral indices are consistent with other experiment, showing a spectral break at around 300 GV with $\approx 1\sigma$ significance level, which is not high enough to make a definitive conclusion.

1.2 Objectives

The objectives of this study are to

- To indirectly measure the CR proton spectrum between approximately 60 – 1000 GV in rigidity.
- To build on the results from the previous study with more dataset
- To improve the optimization technique by using the heuristical methodology
- To reduce the calculation time by inventing a new parallel code in low level from scratch

1.3 Outline of thesis

The dissertation provides various information from the overview introductory context to the technical detail employed in this study as well as the results and interpretations. It is structured as follows.

Chapter I provides the overview and objectives of this work.

Chapter II is the background knowledge relating to this study. This chapter also provides brief history of cosmic ray research which contains impactful experiments and important findings which have advanced the field. Some theoretical detail will be provided along with the historical discoveries. Subchapters describe in more detail about high-energy astroparticle physics.

Chapter III consists of multiple literature reviews involving the study to clarify the theoretical idea as well as for filling the concepts which are important for our better understanding of the next chapter.

Chapter IV consists of datasets selection, flux calculation , computation optimization and interpretation. The following chapter which is chapter V will be the discussion from the analyzed results. The last chapter

The last chapter (Chapter V) is the final summarization from this study. It composed of the final numerical results and the statistical significance.

CHAPTER II
BACKGROUND

2.1 Cosmic ray

This section discusses the historical discoveries from early studies in the field to the latest high-impact experiments.

2.1.1 History

In 1909, Theodor Wolf conducted the famous experiment that pioneered the study of cosmic rays (CRs) by taking an apparatus to measure the rate of ionization from the ground to the top of the Eiffel Tower in Paris (Gray 1949). The result showed that the ionization rate was increased but the magnitude is much lower than the expectation from the underground radioactivity which provided a clue that the origin of CRs was from outer space rather than from the Earth (Hörandel 2013).

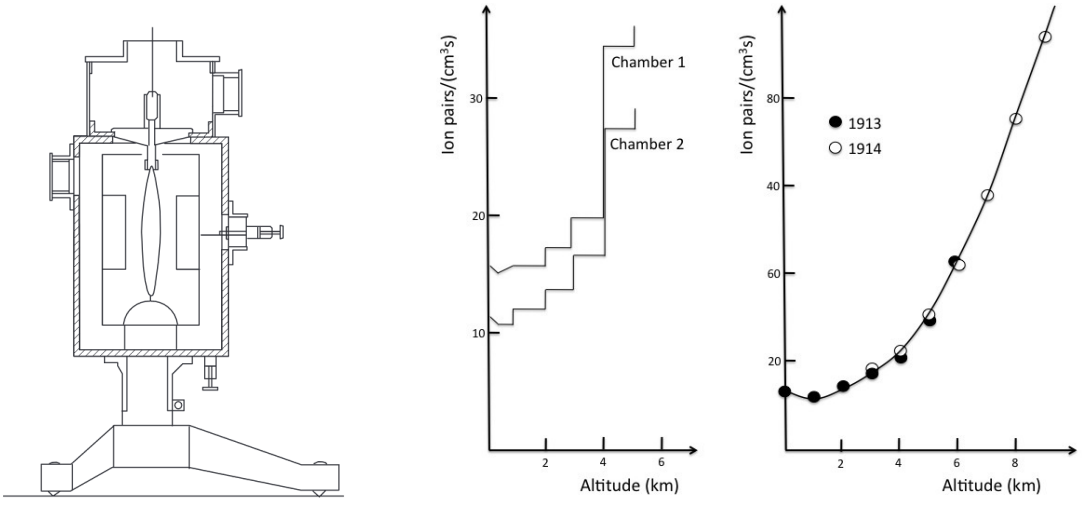

(a) An early version schematic view of electrometer used by Thedor Wulf

(b) Ionization rate from Victor Hess (left) and Werner Kolhörster (right)

Figure 2.1: Wulf's apparatus and the balloon experimental results

However, the experiment measuring the effect of altitude variation with a tiny altitude scale compared to the Earth's atmospheric thickness may not provide enough data. They found that the ionization rate has increased by a quarter compared to that at ground level (De Angelis 2014). Three years later, a risky investigation was conducted by an Australian gentleman who brought a detector and himself to fly with a balloon. His name is Victor Hess, and his name went so famous because he risked his life with the experiment and his flying over 5 kilometers above the ground (Hess 1912). The result is strongly significant and impactful to the astrophysical research community. Risking life In 1914, Werner Kolhörster repeated the balloon experiment with higher altitude up to 9 kilometers from sea level and the ionization rate still increased when the ballon flew higher. These results emphasized that the source of the ionizing ray came from Earth's upper atmosphere or the outer space.

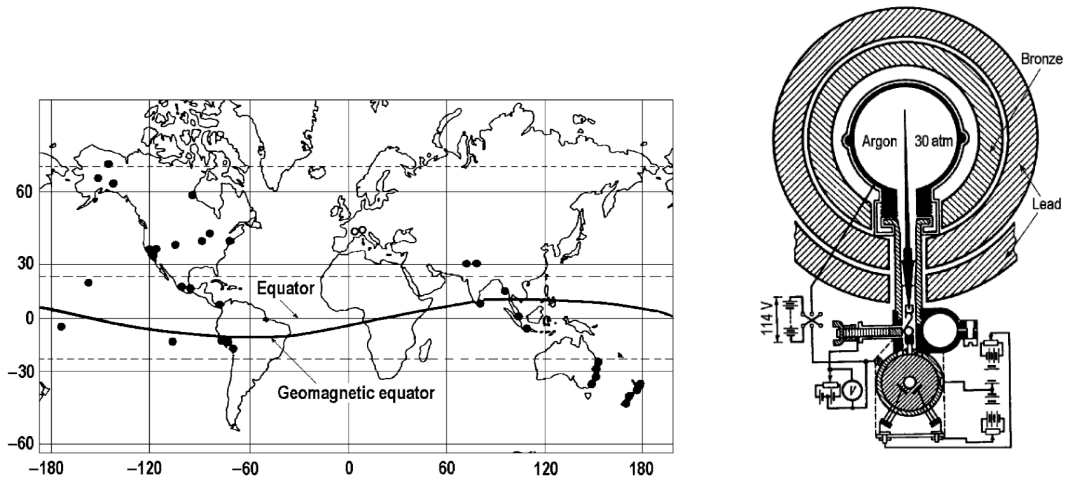

Figure 2.2: (left) Clay's experiment on the geographical variation of CR intensity. Main locations where CR intensity was measured during 8 Compton's expeditions in 1932. (right) The Pb-shielded ionization chamber, organized by Compton. Image is taken from Dorman (2009)

Not only does the ionization rate varies with altitude, the measured rate also depends on the geographical locations. The first experiment was done by John Clay who sailed the ship across the ocean from Holland to Java (Clay 1927, 1928). The geographical locations where CR intensities were measured and the apparatus schematical draft are shown in Figure 2.2. The result shows that

the further from the equator, the higher CR intensity. Another exploration for the geographic variation was done by John Compton in the following five years. He sailed the ship from Sydney (southern hemisphere) to Vancouver (northern hemisphere) for various seasons from 1936 to 1937 back and forth (Compton & Turner 1937). Figure 2.3 demonstrates the latitude variation and the seasonality effects of the multiple trips from the experiment.

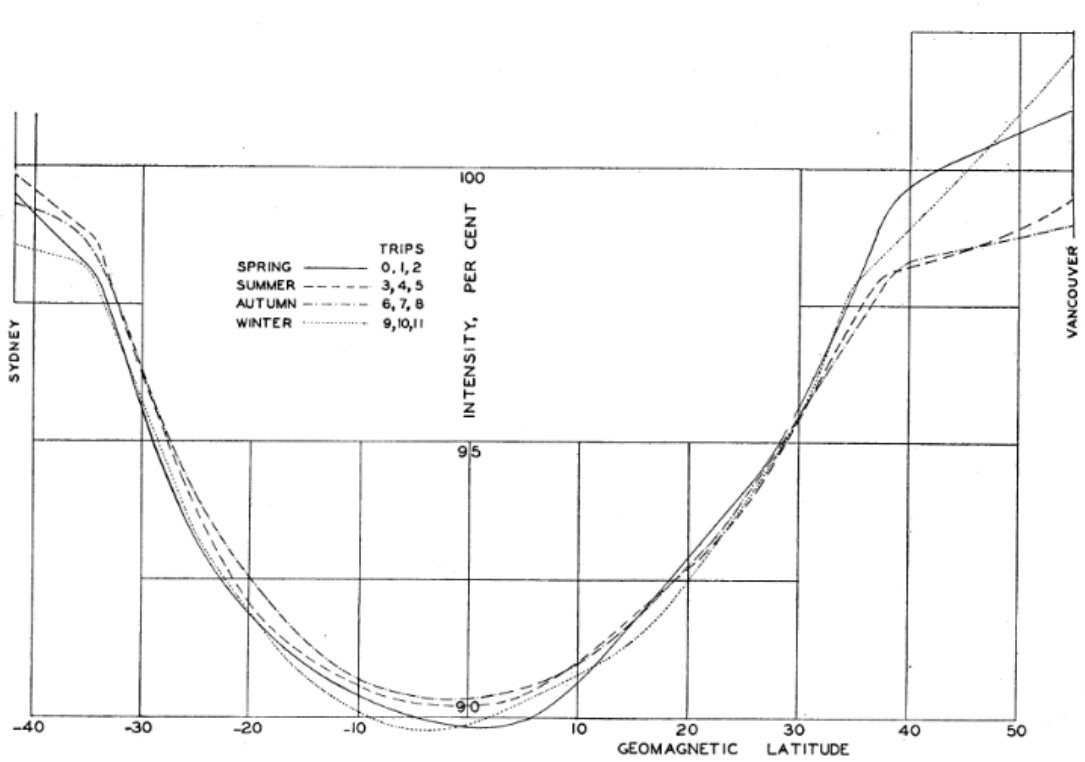

Figure 2.3: Latitude variation of CR intensity for various seasons (Compton & Turner 1937)

The first interpretation study from the discovery has been done by Störmer (1934). The explanation of the CR's altitude variation came from the trajectory of CR particles due to geomagnetic field. In that period, the topic of the geomagnetic field effects on CRs were quite famous. Another impactful study of the CR trajectories under the influence of the Earth's magnetic field was conducted by Bruno Rossi. He studied an assymetry of the East-West distribution of CR flux due to the Lorentz force effects on charged particles by the Earth's magnetic field. He found that the flux is enhanced from the West and interpreted that CRs are predominantly positively charged (Rossi & Greisen 1941).

2.1.2 Physical properties

CRs are high-energy particles propagating through space. CRs gain their momentum from various acceleration mechanisms CRs gain their momentum such as supernovae, created by astrophysical objects. The composition of CRs consists of approximately 90% protons, 8% alphas, and other nuclei of heavier elements (Dembinski et al. 2017). Experimentally, many observations indicate that the CR spectra for all particles and individually do follow the power law in rigidity (momentum per charge) for which the spectral index depends on the energy range. Theoretically, the observed spectrum in a broad energy range is the superposition of CRs produced by various types of sources which could exhibit different spectral indices depending on their physical properties.

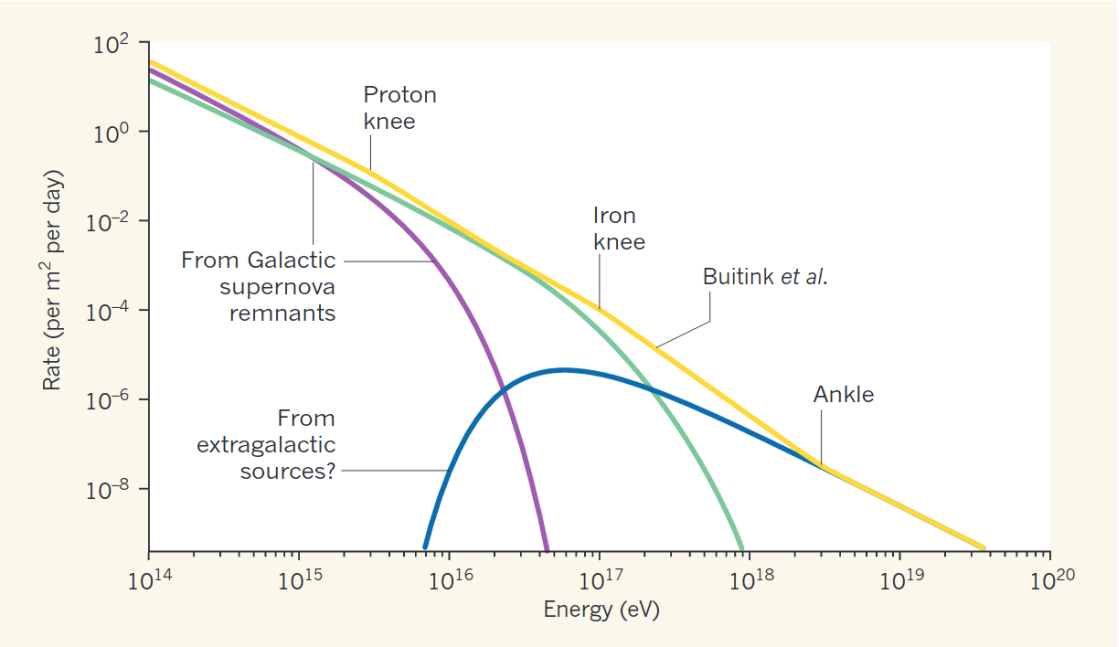

Figure 2.4: The CR spectrum showing the superposition of different populations of sources (Taylor 2016)

Figure 2.4 shows the widely accepted scenario of how each population of CR sources dominates the value of the spectral index for different energy ranges. Three well-established spectral breaking points are the first knee at $\sim 10^{15}$ eV, the second knee at $\sim 10^{17}$ eV, and the ankle at $\sim 10^{19}$ eV. The rate to find one particle with the energy above the first knee is around one particle per square meter per year and the possibility that an apparatus could detect a particle at energy above

the ankle is roughly one particle per kilometer per year.

Interestingly, the maximum energy of UHECRs ever detected never exceed ∼2 orders of magnitude above the ankle energy. This upper energy limit of CRs is widely known as the Greisen–Zatsepin–Kuzmin (GZK limit). According to the GZK theory, UHECRs cannot have an energy above a certain limit because UHECRs are produced from distant extragalactic sources and propagate through vast space full of low-energy background photons, the cosmic microwave background. According to the GZK theory, UHECRs cannot have an energy above a certain limit because UHECRs are produced from distant extragalactic sources and propagate through vast space full of low-energy background photons, the cosmic microwave background. When the energy of the UHECRs is above a certain threshold, they would interact with the background photons and lose their energies (Greisen 1966).

CRs can be categorized into two types based on how they are produced:

1. **Primary cosmic rays**: are produced from astrophysical objects which may be within the Solar system, within the Milky Way Galaxy (Galactic CRs), or from extragalactic sources (extragalactic CRs). Some example origins of primary CRs are stellar winds, supernovae, pulsars, active galactic nuclei, and speculative sources such as dark matter decay.

2. **Secondary cosmic rays**: are produced from primary CRs interacting with the Earth's atmosphere. The interactions create showers of hadronic, leptonic, and electromagnetic particles. Researchers have developed and improved Monte Carlo simulations of the CR air showers based on particle physics theory. These models are very useful for secondary CRs studies.

2.1.3 γ-ray production

The production mechanisms of γ rays are fundamentally different from those for charged particles that can be accelerated with the electromagnetic force. While charged particles can gain or lose energy during their propagation through space, high-energy γ-ray photons tend to only lose energy. Here we briefly discuss the production processes of γ rays.

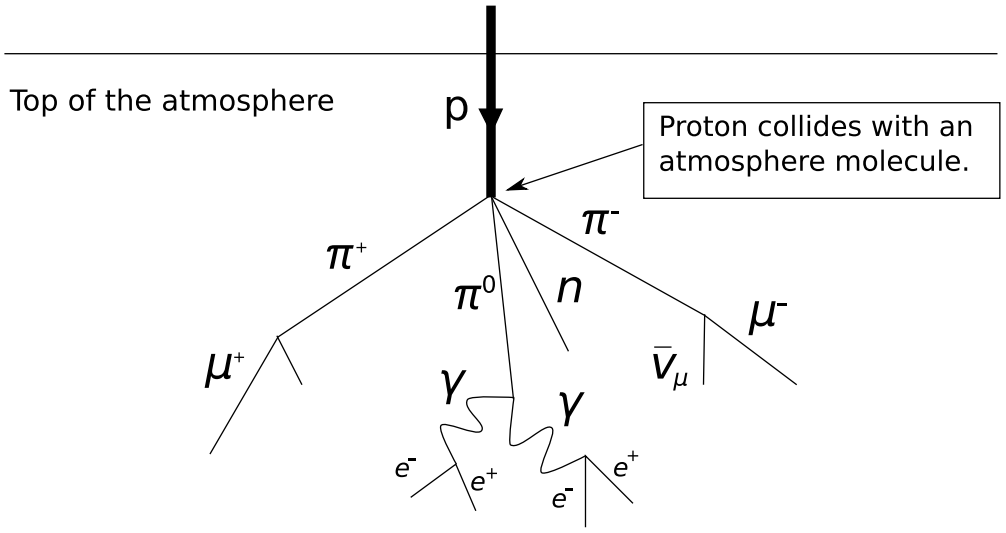

Figure 2.5: Simplified schematic of CR proton air shower (Image taken from Cosmic Rays, Wikipedia, Magnus Manske, 2011)

- **Decaying of unstable matter**: Radioactive decay is one of the most well-known phenomena for the γ-decay mode. One example of heavy-ion decay is cobalt-60. It decays into an excited state of nickel as

  $$^{60}_{27}\mathrm{Co} \longrightarrow {}^{60}_{28}\mathrm{Ni}^{*} + \mathrm{e}^{-} + \bar{\nu} + \gamma\,,$$

  then the excited nickel emits another γ ray to become the stable state

  $$^{60}_{28}\mathrm{Ni}^{*} \longrightarrow {}^{60}_{28}\mathrm{Ni} + \gamma\,.$$

  Some particles, such as the neutral pion (π^0), decay into γ rays. The Feynman's diagram of a π^0 decay is demonstrated in Figure 2.6. The lifetime of π^0 is short, $\sim 8.5 \times 10^{-17}$ seconds. There are some other decay channels

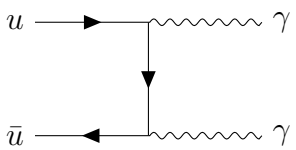

Figure 2.6: Feynman's diagram of the neutral pion (π^0) decay into two γ-rays.

  (with $< 1\%$ branching ratio) that result in combinations of a photon and pairs of lightweight leptons, as long as the momentum, energy, and quantum numbers are conserved. Another interesting property of the $\pi^0 \to 2\gamma$ mode is the momentum vectors of the γ-ray pair have the same magnitude but

opposite direction in the rest frame of π^0.

- **electron–positron annihilation**: Electron (e^-) and positron (e^+) are the lightest leptons which can annihilate into 2 γ-rays. Heavier and shorter-lived leptons, muon (μ) and tau (τ), can also create γ rays in a similar manner as illustrated in Figure 2.7.

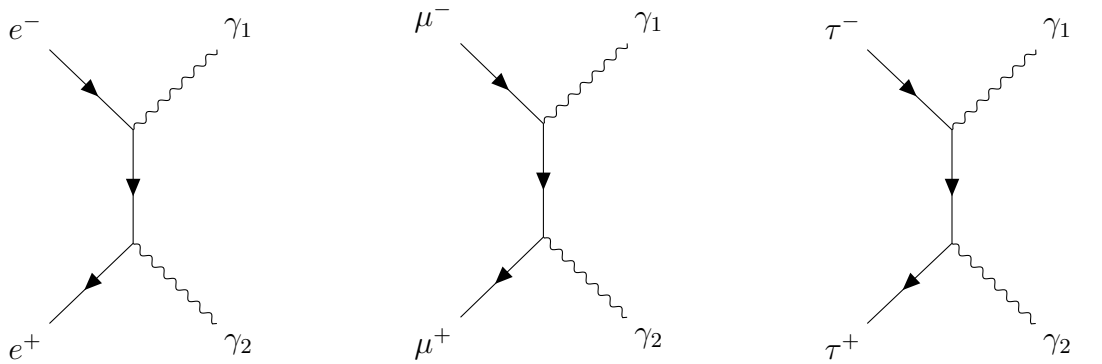

(a) Lightweight leptons (b) Mediumweight leptons (c) Heavyweight leptons

Figure 2.7: Lepton-antilepton annihilation path diagram.

- **Synchrotron & Bremsstrahlung radiation**: It is theoretically and experimentally well known that when charged particles are accelerated, they emit photons. If the acceleration is due to a magnetic field, the emission is called the synchrotron radiation. Humans have built donut-shaped apparatuses inside which charged particles are traveling in a circle guided by strong magnetic fields and produce synchrotron radiation for various applications.

  Another closely related mechanism is the Bremsstrahlung process. When charged particles, typically electrons, move close to heavier positively charged nuclei, the Coulomb force between them cause an acceleration on the electrons, resulting in Bremsstrahlung radiation.

- **Inverse Compton scattering**

  scattering: A photon can electromagnetically interact with an electron (or any charged particles). The Compton scattering describes a photon losing its energy to an electron. In the opposite situation, a highly relativistic electron

can interact and transfer its energy to a low-energy photon to become a γ-ray photon. This process is called the "Inverse Compton scattering" as shown in Feynman's diagram in Figure 2.8.

(a) First branch (b) Second branch

Figure 2.8: First-order Feynman's diagrams for the Compton and Inverse Compton processes.

Astrophysical sources of γ rays

- **Supernova remnants (SNRs) and molecular clouds**: The supernova is a violent explosion of a dead star, causing the material to expand in a spherical shell that sweeps the interstellar medium and decelerates over time. The shock wave from the explosion is believed to produce the shock acceleration of CRs. Three major γ-ray production processes from the SNRs involve hadronic (mostly π^0 decay) cascades, electron bremsstrahlung, and Inverse Compton scattering (Dermer & Powale 2013).

- **Diffused γ-ray emission from the galactic plane**: The plane of the Milky Way galaxy has a high density of gas, dust, stars, and other types of objects. Thus, CRs can interact with such material and create diffuse emission of γ rays, which is brighter along the Galactic plane as illustrated in Figure 2.9.

- **Pulsars**: Pulsars are rapidly spinning neutron stars as a result of the supernova explosion of massive stars. They have very strong magnetic fields and can emit bright radiation in a beam from their magnetic poles. The pulsars' intensity could appear to be a periodic emission to observers on Earth due to the pulsars' rotation. They are likely the majority of point sources in

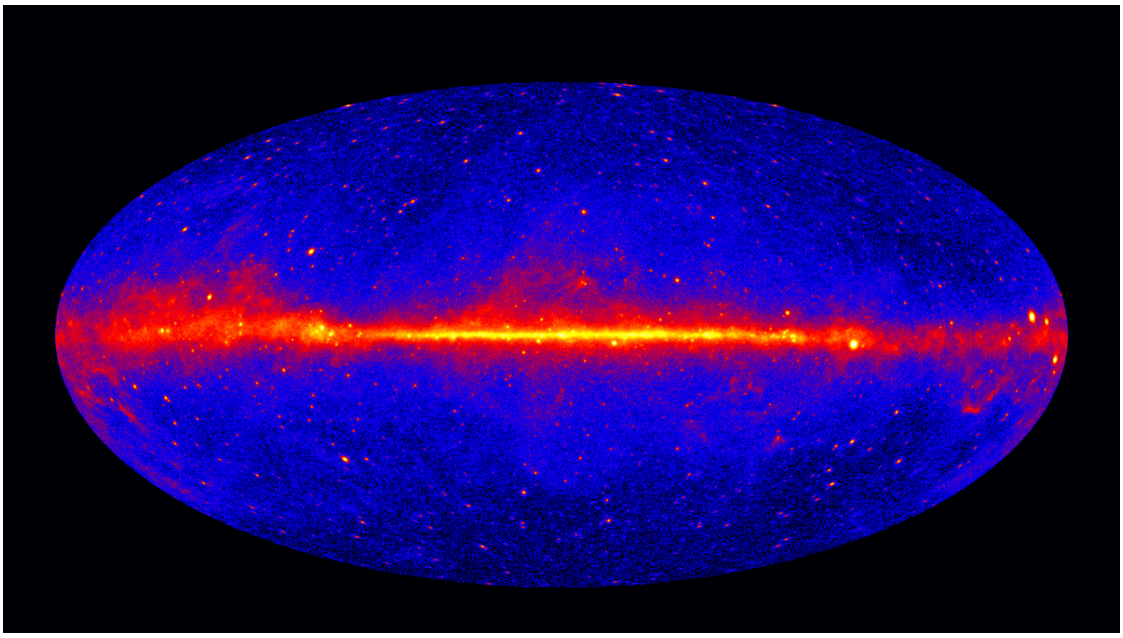

Figure 2.9: Intensity of γ-ray $>$ 1 GeV in galactic coordinates (Image credit: NASA/DOE/*Fermi* LAT Collaboration).

the Galactic plane region detected by *Fermi* LAT.

- **Active Galactic Nuclei (AGNs)**: AGN is the center of the active galaxy. The luminosity is much higher than the stars. It produces multi-wavelengths photon in a different band such as radio, microwave, γ-ray and etc. Then this object could be observed from various instruments.

- **Earth's limb γ-ray production**: The closest γ-ray source to the LAT is our Earth's atmosphere. The Earth's upper atmosphere is extremely bright in γ-ray band. The Earth shines in high energy (>100 MeV) γ ray due to the collisions of CRs with the Earth's upper atmosphere producing secondary particles which include π^0's that quickly decay into γ rays. The Earth's γ-ray emission is the main target source for this study.

2.2 *Fermi* Large Area Telescope (LAT)

One of the famous space telescopes that observes the sky in γ-ray wavelength is the *Fermi* Large Area Telescope (LAT). Formerly, it was called

Gamma-ray Large Area Space Telescope (GLAST). The LAT is designed to collect high-energy (∼100 MeV to above 300 GeV) photons data, but it is also able to measure electrons. The orbiting radius is around 550 kilometers from sea level. *Fermi* also carries the Gamma-ray Burst Monitor (GBM) to study γ-ray bursts for seeking exotic events. The telescope was launched on 11 June 2008 and is still currently taking data in 2021.

2.2.1 Overview

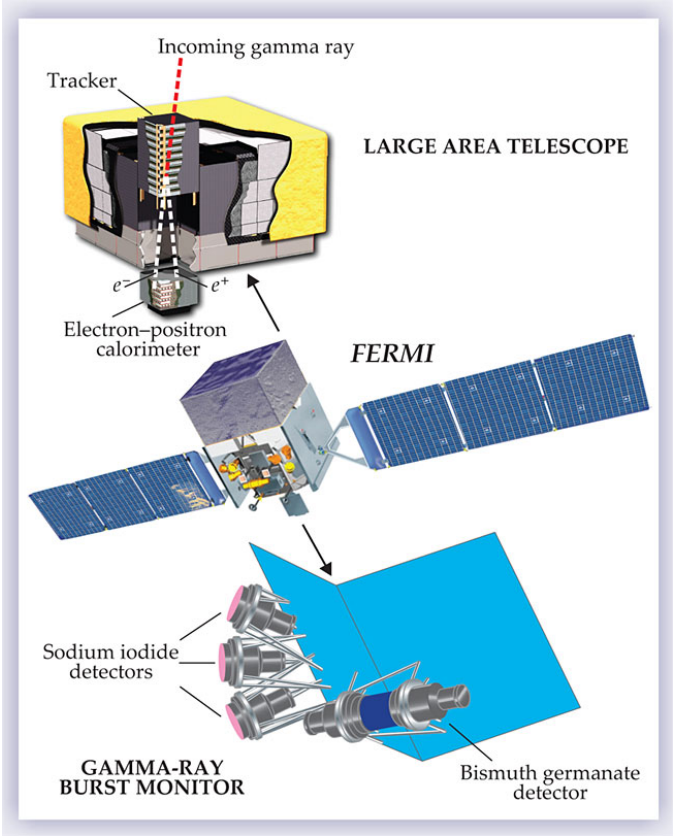

Figure 2.10: Main components of the LAT and the GBM on the *Fermi* Space Telescope (Michelson et al. 2010)

Figure 2.10 shows components of *Fermi*. There are two instruments onboard: the Large Area Telescope (LAT) and the Gamma-ray Burst Monitor (GBM). The LAT is the primary instrument that detects γ rays between ∼100 MeV to above 300 GeV. The GBM monitors the sky at a lower energy range of ∼8 keV to 40 MeV. The GBM consists of two sub-components which are sodium iodide

detector for low-energy photons (8 keV to 1 MeV) and bismuth germanate detector for high-energy photons (0.2 MeV to 40 MeV). The GBM monitors transient events and immediately triggers the LAT to point to the locations of the flares for a certain period of time before returning to the normal survey mode.

2.2.2 Large Area Telescope (LAT)

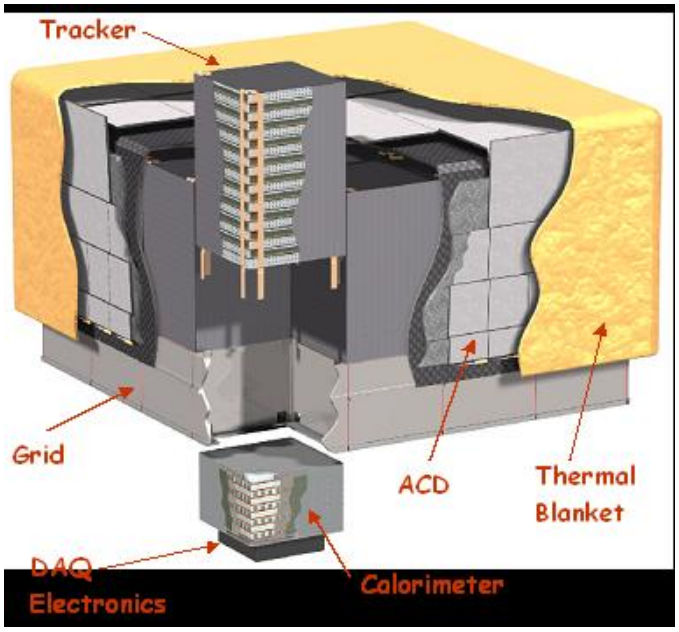

Figure 2.11: Main components of the LAT (Image taken from https://fermi.gsfc.nasa.gov)

Figure 2.11 illustrates main components of the LAT which are described as follows.

Anti-coincidence Detector (ACD)

The ACD consists of 89 plastic scintillator tiles covering four sides and the top of the LAT. Each tile contains two photomultipliers and wavelength shifting fibers embedded in the scintillator. The edges of neighboring tiles are overlapping to reduce the effect of the gaps. The main objective of the ACD is to reject background charged particles which create electrical signals when passing through the scintillator tiles. The estimated efficiency for charged particle identification by the ACD is about 0.9997.

Tracker (TKR)

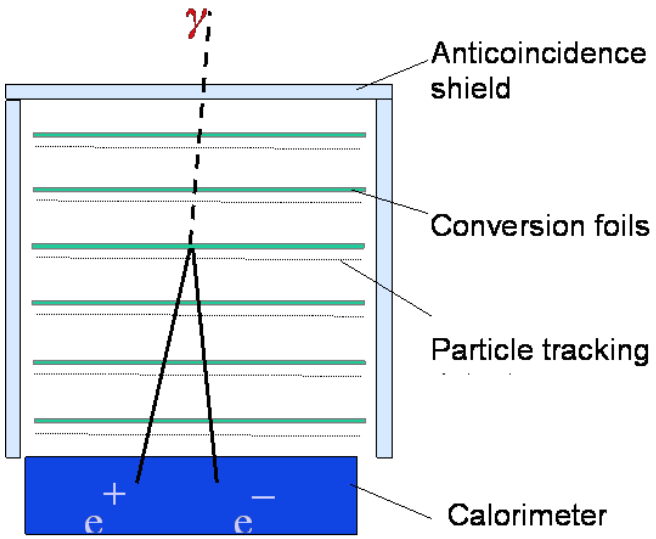

Figure 2.12: Schematic of γ-ray detection of the LAT (Image taken from https://fermi.gsfc.nasa.gov)

The TKR system consists of 16 planes of particle tracking detectors made from silicon strips which are interleaved with tungsten conversion foils as shown in Figure 2.12. An incident γ ray has high probability to interact with the conversion foil and is converted into an e^+e^- pair.

As the e^+e^- pair travel through the silicon strip trackers, they leave their traces on the position sensing detectors, allowing us to reconstruct the direction of the original photon. The narrow gaps between layers of silicon trackers improve the angular resolution of the LAT compared to previous instruments. In Figure 2.13, case (a) is the typical situation in which photon is pair-produced by the conversion layer and clean e^+e^- footprints are recorded. Nevertheless, there are some cases, such as (d) in which the e^+e- paths pass through the gap between towers or (e) in which the photon is pair-converted outside of the conversion foil. Having multiple layers of trackers helps the reconstruction of these special cases.

Calorimeter (CAL)

When the e^+e^- pair enters the CAL, they radiate their energy in the CsI crystal scintillators, producing electronic readout which is proportional to the

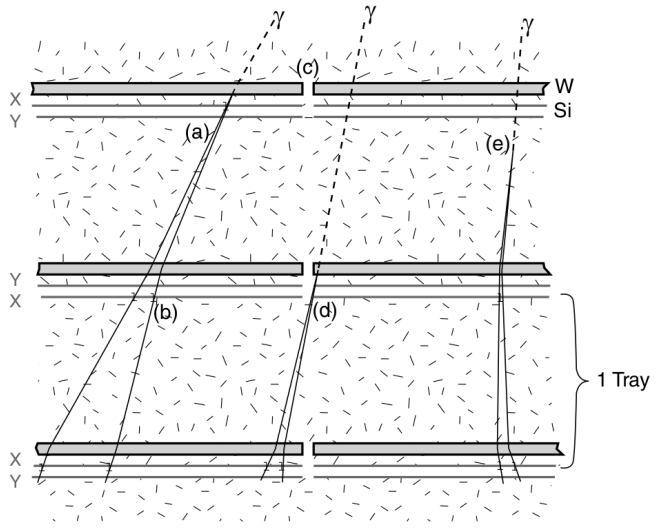

Figure 2.13: LAT's particle tracker. (a) The ideal case where the conversion happens in an early layer and leaves a footprint along with multiple layers (b). (c) The photon skips the first layer and be converted in another layer with a missed hit in 1st and 2nd of Si trackers (d). (e) Conversion occurs in structural materials and is traced by the following Si trackers. (Atwood et al. 2009)

energy loss of e^+e^- inside the CAL. According to the radiation lengths of e^+ and e^-, the CAL is optimized to contain the e^+e^- showers with energy from 0.1 to a few hundred GeV. Thus, TeV photons could have large uncertainties in their energy reconstruction by the LAT.

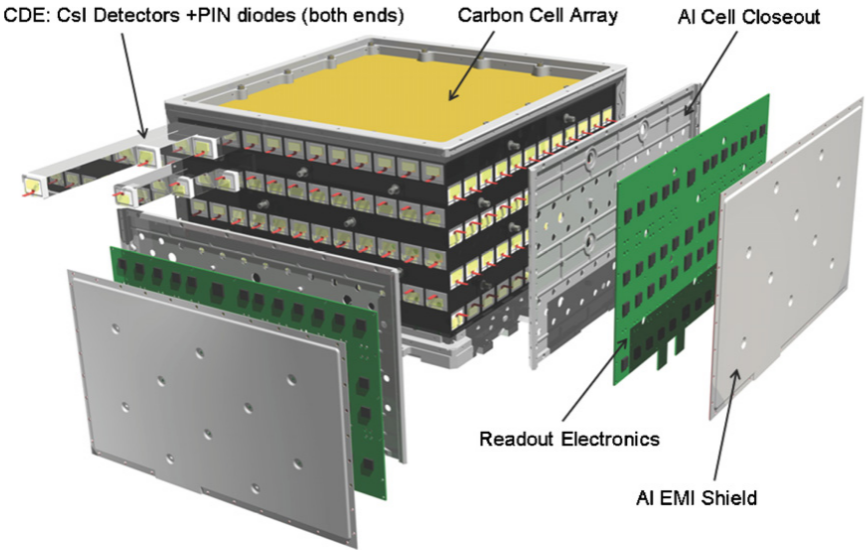

Figure 2.14: LAT's calorimeter (Atwood et al. 2009)

The overview apparatus structure is illustrated in Figure 2.14. Each calorimeter module consists of 96 CsI(Tl) scintillator crystals with the size of 2.7 cm x 2.0 cm x 32.6 cm and PIN photodiodes at both ends which connect to the readout electronic components translating the amount of light sparkled in the crystal to digitized signals. Each horizontal layer is combined from 12 crystal components and stack 8 times by rotating them 90°each for boosting the angular resolution for the sparking lights. A carbon cell was build for supporting the structure of low mass particle tracker due to the properties of high stiffness, thermal conductivity and thermal stability. An electron, position, or γ-ray will deposit the energy in the calorimeter as the scintillated lights via electromagnetic interactions. The segmented crystal allow LAT to trace the showers of particles for spatial imaging.

Data Acquisition System (DAQ)

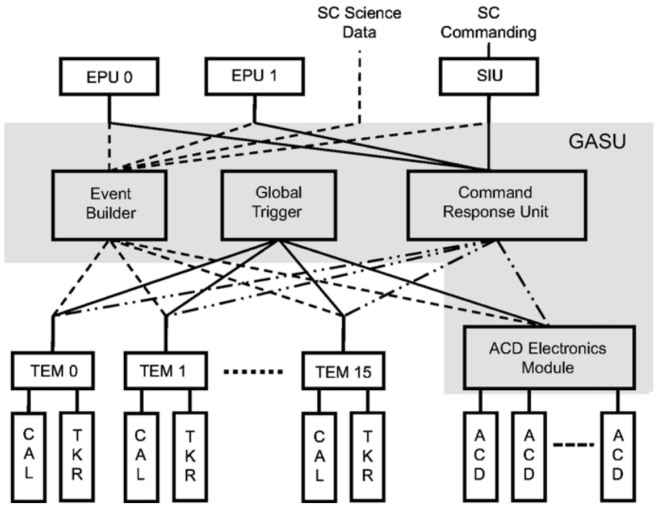

Figure 2.15: Flow chart of LAT's data acquisition system (DAQ) (Image taken from Atwood et al. 2009)

The DAQ system is designed to reduce the amount of raw data transmitted to the ground through the limited bandwidth. The lowest-level components are tower electronic modules (TEMs) to serve as the interface for the the TKR and CAL. All TEMs create event buffering and communicate with the Event Builder Module (EBM) which is a component of Global-trigger/ACD-module/Signal Distribution Unit (GASU). Command Response Unit (CRU) is built to communicate the software

execution in the DAQ system. Lastly, the Event Processing Unit (EPU) processes a selected event from TEM and ACD Electronics Module (AEM). Filtering an event could reduce the data transmission rate from a few kHz to around 400 Hz to the ground level.

2.2.3 Event reconstruction

Before launch, the event reconstruction algorithm for photons was based entirely on the Monte Carlo (MC) simulations by modeling the photon and background signals in the ACD, TKR, and CAL systems in realistic in-orbit environment. The data processed by this pre-launch event reconstruction algorithm is called "Pass 6" version.

The raw onboard data are called "level 0". After transmitted to the ground and processed, the data become "level 1". After a few years after launch, the LAT collaboration has improved the event reconstruction algorithm and released the "Pass 7" version based on the actual in-flight data. The newest version and likely to be the final version is Pass 8. In each version, photons are organized into different classes (e.g., TRANSIENT, SOURCE, ULTRACLEAN, ULTRACLEANVETO) based on the level of background contamination. The TRANSIENT class has the loosest selection which allows us to obtain better statistics for the observations of faint transient sources but with a trade-off for the highest probability of background contamination. The SOURCE class is optimized for typical source analyses of the LAT, while the ULTRACLEANVETO is the cleanest class with low background contamination but also with the lowest statistics.

2.2.4 LAT performance and characteristics

Fermi LAT's physical cross-section area is 1.8 x 1.8 m^2. However, its effective area for particle detection varies as a function of energy and incidence angle. Figure 2.16 shows the LAT's Pass 8 SOURCE effective area for photons arriving perpendicular to the cross section of the LAT as a function of energy, indicating low detection efficiency below ∼100 MeV and above ∼1 TeV. The effective area

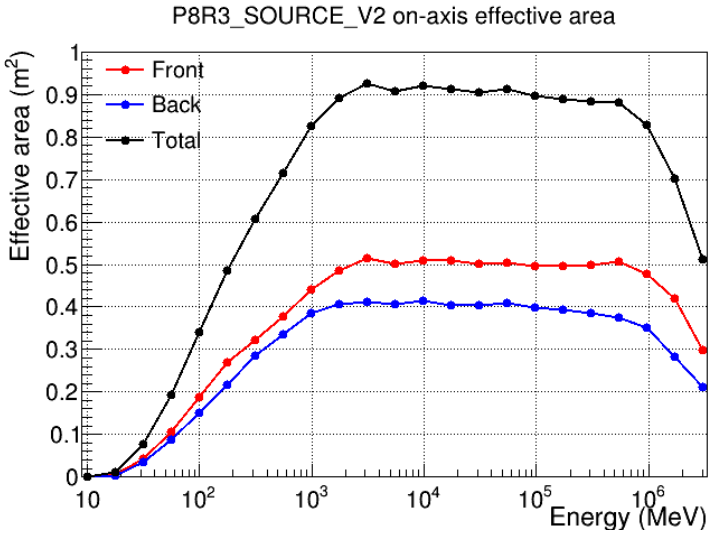

Figure 2.16: LAT's effective area as a function of energy for normally incidence photons (Maldera 2019). Front means the effective area of an event that photon hits the conversion layer at the top and decays into a pair of electron-position. Back represents the effective area of the event that photons pass through the top part and be converted to the bottom of the TKR module. The total effective area (black) is the combination of front and back.

from front part is higher than the back due to the conversion event that happens in the front leaves more footprint in silicon strip of TKR more than the back.

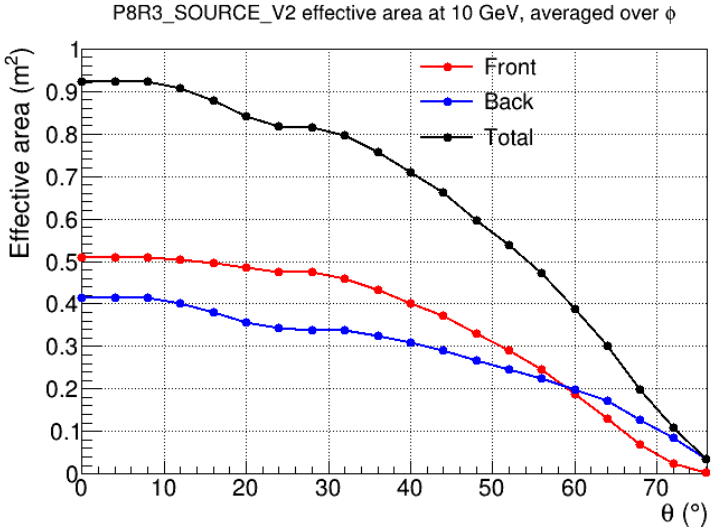

Figure 2.17: Effective area versus incidence angle (Maldera 2019)

Another crucial variable relating to the LAT effectiveness is the incidence angle (θ_{LAT}). An event with small θ_{LAT} would pass through many tracking layers, yielding better detection efficiency. Figure 2.17 shows the relation between the

effective area and θ_{LAT}.

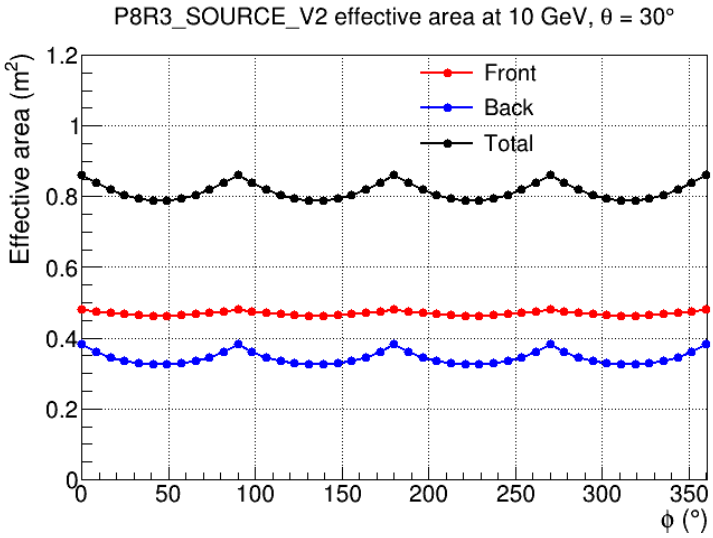

Figure 2.18: Effective area versus ϕ_{LAT} (Maldera 2019)

Since the structure of the LAT is cube-like, the effective area, therefore, depends on the azimuthal angle (ϕ_{LAT}) of the photon. Figure 2.18 illustrates the asymmetry of the LAT's effective area as a function of ϕ_{LAT}, showing four peaks corresponding to corners of the LAT.

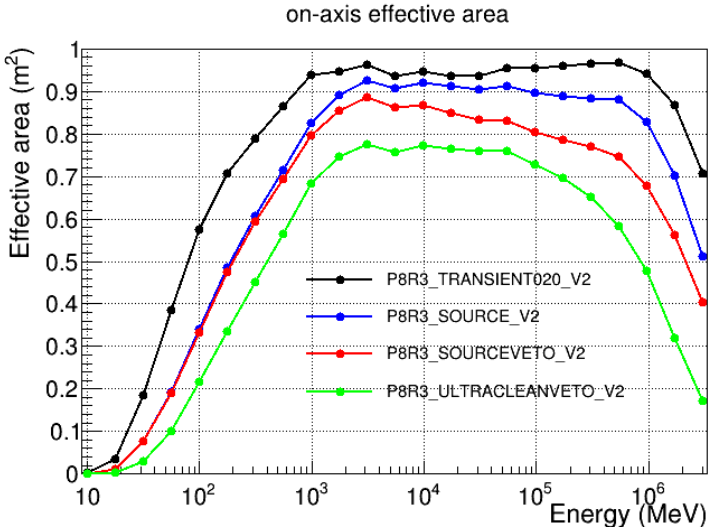

Figure 2.19: Effective area along with the energy of each event class (Maldera 2019)

The event class also has a crucial role when considering the effectiveness of the reconstructed event. The cleanest class namely "ULTRACLEANVETO" would have the smallest effective area. On the other hand, the TRANSIENT

class would yield the largest effective area as illustrated in Figure 2.19. Please see Appendix G for the illustration of the effective area from class "ULTRACLEANVETO" that has been selected in this work.

CHAPTER III
LITERATURE REVIEW

3.1 Cosmic ray

CRs could come from different origins from galactic to extra-galactic sources. Relatively low-energy (below a few GeVs) CRs from the Sun known as the "solar energetic particles" are produced from the coronal mass ejection event in which ions are dragged by a turbulent magnetic field in the plasma. On the other end of the spectrum, extremely high-energy (above EeV) CRs are likely from extragalactic supermassive blackholes. The dominant Galactic sources of TeV CRs are hypothetically supernova remnants (SNRs). The theoretical description of acceleration in SNR and solar flares is the shock wave acceleration in the following paragraph.

One of the most impactful studies of CR's acceleration mechanism was conducted by Fermi (1949). The study describes how high-energy CR particles gain large momentum from the shock wave that was generated by supernovae or violent explosions of massive stars. This acceleration model is known as the diffusive shock acceleration process which provides the correct description of the spectrum as a power law in rigidity. At high-energy, the rigidity is approximately directly proportional to the total energy (E). Thus, the CR spectum can be modeled in the form

$$\frac{dN(E)}{dE} \propto E^{-\gamma} \tag{3.1}$$

where $\gamma \geq 2$. However, moving magnetized plasma cloud can accelerate the charged particle in the space called "second-order Fermi acceleration". Both regimes can be computed using the Lorentzian forces regardless of thermal collision in the process.

CR protons are major components in the arrival of CR particles under multiple observations. However, *alpha* particles (He nuclei) are the second most abundant CR particles and should be taken into account in the calculations of CR interactions. The other major nuclei in CRs are C, O, Ne and so on. Differential fluxes in kinetic energy for various nuclei from multiple experiments are visualized in Figure 3.1 by Beringer et al. (2012).

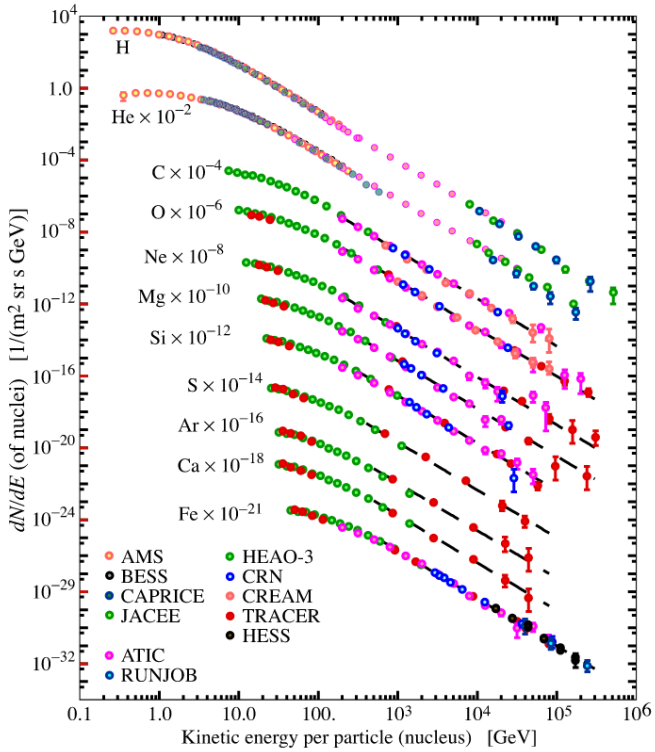

Figure 3.1: CR elemental spectra from various experiments (Beringer et al. 2012)

Moving plasmas inside the Earth generate the geomagnetic field for which the north pole is at the geographical south pole of the Earth and vice versa. The Earth's magnetic field plays an important role in the arrival of CR particles because the Lorentzian forces could bend the direction of a moving charged particle depending on the rigidity of the particle.

Firstly, the geomagnetic field creates the CR cutoff rigidity which is the minimum rigidity of incident charged CRs to arrive at the top of the atmosphere at different locations on Earth. Figure 3.2 shows a cutoff rigidity on the Earth's surface.

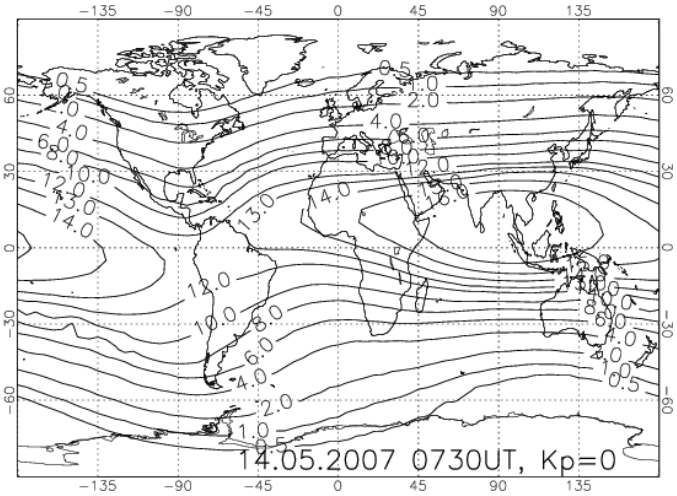

Figure 3.2: World map with computed geomagnetic vertical cutoff rigidity contour lines on a given date (Ütikofer 2007)

Secondly, due to the centripetal Lorentz force, charged CRs would spiral around magnetic field lines, creating the so-called "East-West effect" which results in the higher flux of CRs arriving from the West than that from the East for detectors in the low-Earth orbtis. Historically, the detection of the East-West asymmetry of CRs by Rossi in 1930s (Rossi 1934) provided the first clue that CRs are predominantly charged.

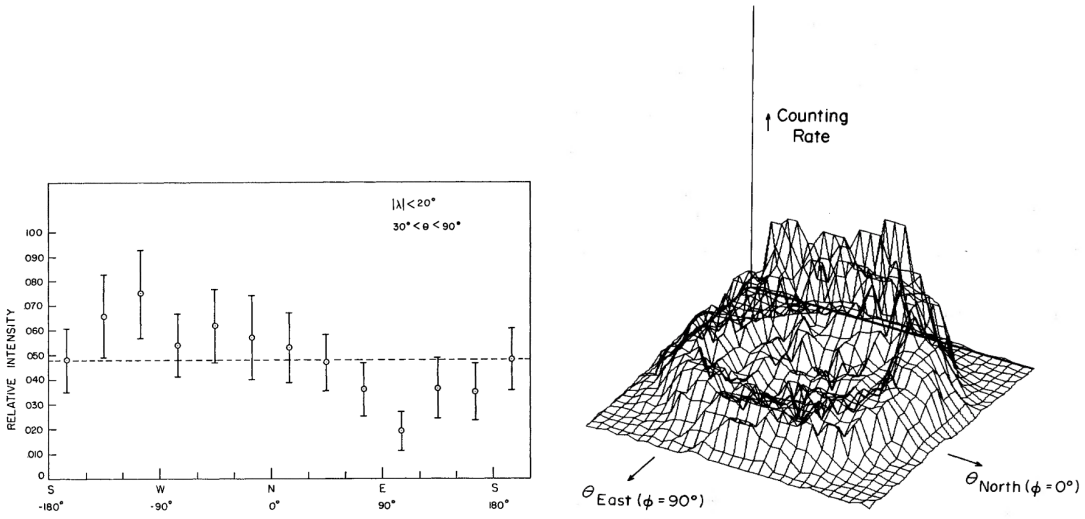

(a) Explorer XI (Kraushaar et al. 1965) (b) OSO-3 (Kraushaar et al. 1972)

Figure 3.3: The East-West asymmetry of the Earth's γ-ray intensity

3.2 Earth's γ-ray

When CRs interact with the Earth's upper atmosphere, hadronic showers of secondary particles including π^0's are produced which then quickly decay into γ rays. This CR-induced γ-ray emission makes the Earth by far the brightest γ-ray source for space-based detectors due to the proximity. The pioneering cosmic γ-ray experiment in space was conducted by Kraushaar et al. (1965) by deploying a γ-ray detector onboard the Explorer XI satellite. This experiment clearly detected the Earth's γ-ray emission and showed distinguishable intensity from the East and West as shown in Figure 3.3a. The third Orbiting Solar Observatory (OSO-3) was the second experiment which observed MeV-range γ rays and studied the Earth's emission (reference). The 2-D plot of the Earth's γ-ray intensity is shown in Figure 3.3b.

Moreover, Kraushaar et al. (1965) found the strong enhancement in the γ-ray intensity in the direction near the Earth's horizon (or limb) as shown in Figure 3.4a due to CRs grazing tangentially through the Earth's upper atmosphere and forward scattering photons towards the detector. The observed intensity also depends on the geomagnetic latitude location of the satellite as shown in Figure 3.4b. Since CR flux declines steeply with rigidity, low-rigidity CRs are much more abundant than high-rigidity ones. Therefore, the CR-induced Earth's γ-ray intensity from high geomagnetic latitude (low cutoff rigidity) is greater than that from the low geomagnetic latitude as shown in Figure 3.4.

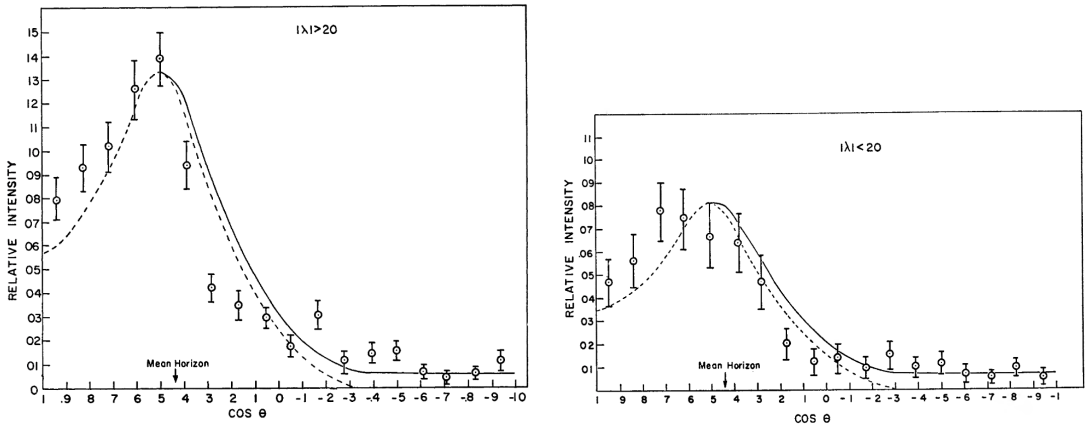

(a) observing above 20°geomagnetic latitude (b) observing below 20°geomagnetic latitude

Figure 3.4: γ-ray intensity along the zenith angle (Kraushaar et al. 1965)

The following experiment of Earth's γ-ray observations was conducted by sending the second small astronomy satellite (SAS-2) with a higher angular resolution at energy above 35 MeV up to GeV range (Thompson et al. 1981). The projected 3-D representation of intensity is shown in Figure 3.5a. A few decades later, another precise γ-ray detector has been attached to the Compton Gamma Ray Observatory (CGRO) satellite (Petry 2005) which observed the bright region around the Earth's limb region as in Figure 3.5b.

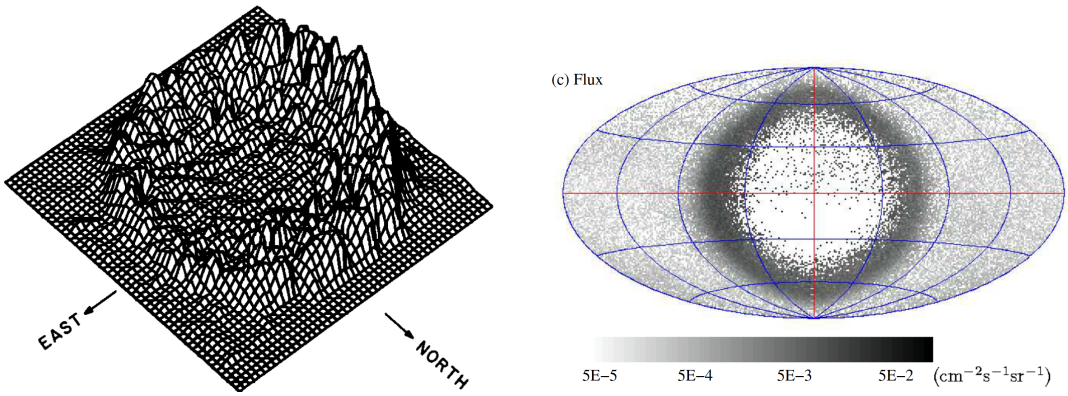

(a) SAS-2 experiment (Thompson et al. 1981) (b) EGRET experiment (Petry 2005)

Figure 3.5: The Earth's centered intensity plot from the satellite based observations

Morris (1984) showed the Earth's γ-ray intensity from different line-of-sight atmospheric depth around the limb region as plotted in Figure 3.6, using data from Thompson et al. (1981). This study computes the γ-ray spectrum from the bright region as seen from the Earth's and lunar limbs. Figure 3.7 shows the spectrum from the theoretical calculation. Figure 3.7a identifies the 2 bounds of the limb's region with an approximated air depth. Solar activities can affact low-energy CR flux within the solar system. This phenomenon can cause noticable change in the γ-ray spectrum as demonstrated in Figure 3.7b.

In 2009, *Fermi* LAT released its first CR-induced Earth's γ-ray emission analysis Abdo et al. (2009). With technological improvements, the LAT is capable of detecting γ rays from 100 MeV to near TeV with high angular resolution. This study shows that the East-West effect is highly depends on the energy. The effect is less prominent at high energy because CRs at high rigidity are not deflected strongly by the Earth's magnetic field as shown in Figure 3.8. In addition, the

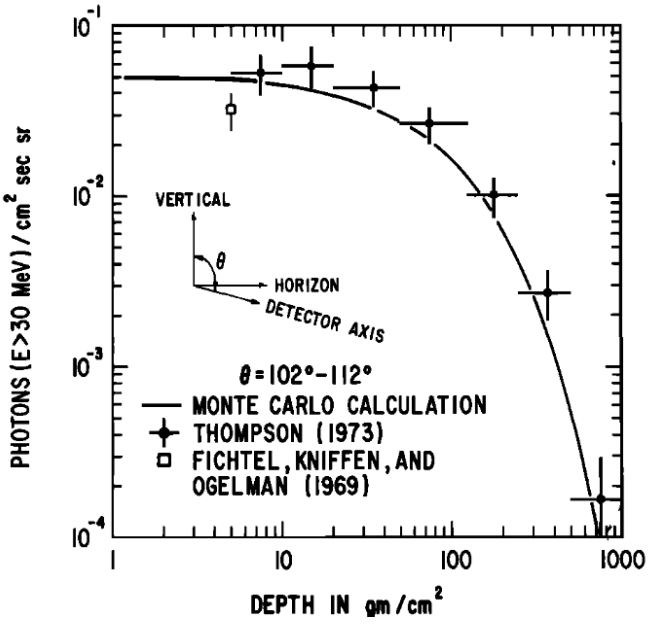

Figure 3.6: Calculated γ-ray intensity at different atmospheric depth (Morris 1984)

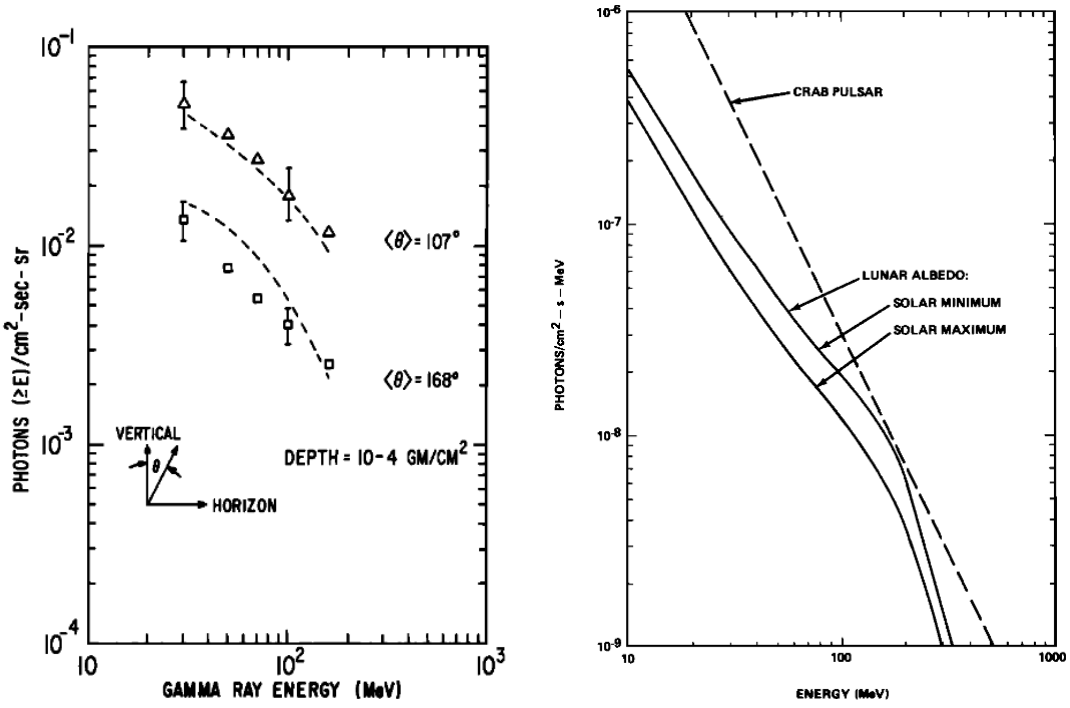

(a) Earth's limb γ-ray spectrum (b) Lunar's atmospheric γ-ray spectrum

Figure 3.7: γ-ray spectrum from proton-nuclei interactions (Morris 1984)

latest study of Earth's γ-ray emission from Madlee et al. (2020) has clearly observed the effect in the spectrum at a few GeV scale.

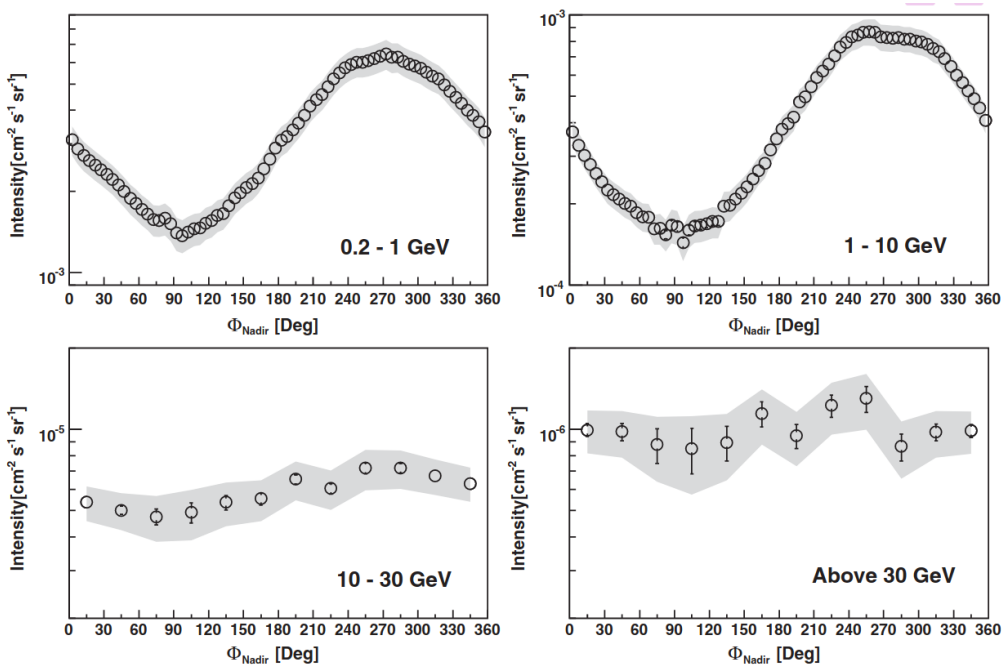

Figure 3.8: γ-rays intensity from limb emission in 4 energy ranges (Abdo et al. 2009)

The objective of this work is to indirectly measure the proton spectrum in the GeV range. The direct measurement in an early study of high-energy CR particles such as proton and helium was performed by Haino et al. (2004). More recently, PAMELA measured the proton and α spectra up to TeV and reported an abrupt break in both spectra at a few hundred GV with high significant level (Adriani et al. 2011).

Although PAMELA claimed that the detection of the spectral break was statistically significant, the break was close to its upper energy limit and an independent confirmation would be important. An indirect measurement of CR proton spectrum has been performed in energy between 90 GeV to 6 TeV by taking advantage of the brightness of Earth's limb γ-ray emission from the collision of incident CR protons (Ackermann et al. 2014). This analysis used 5 years of Earth's γ-ray data along with two proton-proton collision models to investigate the spectral break of CR proton at a few hundred GV which PAMELA reported.

One of the most recent space-based CR detectors, AMS-02, was installed on the International Space Station in 2011 to study antimatter and dark matter

signals in CRs. AMS-02 can detect antimatter such as positrons and antiprotons, and also other heavyweight nuclei such as B, C, N, O, and Ne. In 2015, AMS-02 reported precision measurement of CR proton spectrum and confirmed the spectral break at $\approx$ 340 GV at 99.9% confidence level (Aguilar et al. 2015). The result from AMS-02 is consistent with other direct measurements from balloon-based and space-based experiments as shown in Figure 3.9. In addition, the helium spectrum was also measured and reported in Aguilar et al. (2015).

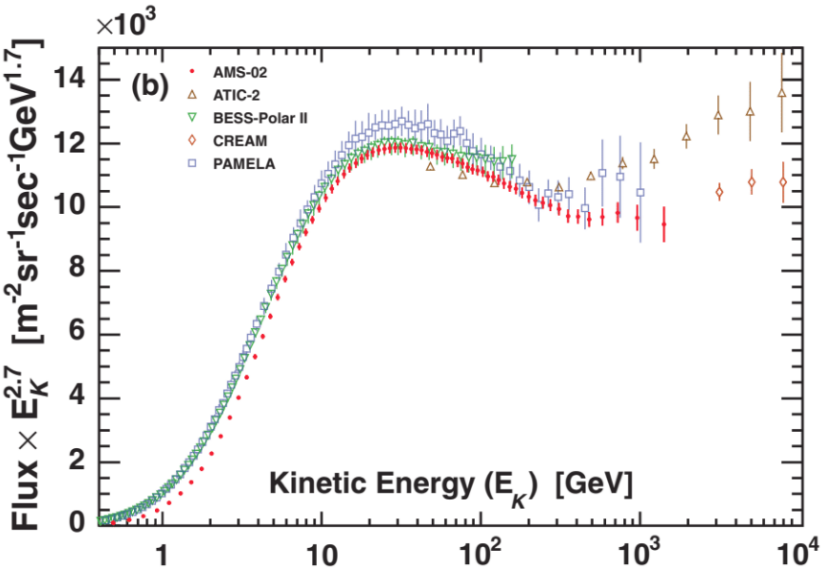

Figure 3.9: CR proton spectrum from AMS-02 and earlier direct measurements (Aguilar et al. 2015)

According to the previous study (Ackermann et al. 2014), the detection of the CR proton spectral break at 300 GV is still at low significant level. In this work, a similar study will be performed with a larger data size from $\sim$ 9 years of observation. Moreover, we improve the analysis process by employing the heuristic optimization as well as using high performance calculation of the exposure maps for faster computational time of the Earth's γ-ray spectrum calculation.

CHAPTER IV
METHODOLOGY

This chapter gives information on γ-ray flux calculation by providing the information on data filtering and the extracting processes. The recent hadronic interaction model yielding γ rays is discussed. This model is used to reconstruct the CR proton spectrum from the measured γ-ray spectrum. Lastly, the last sub-chapter contains details of statistical analysis.

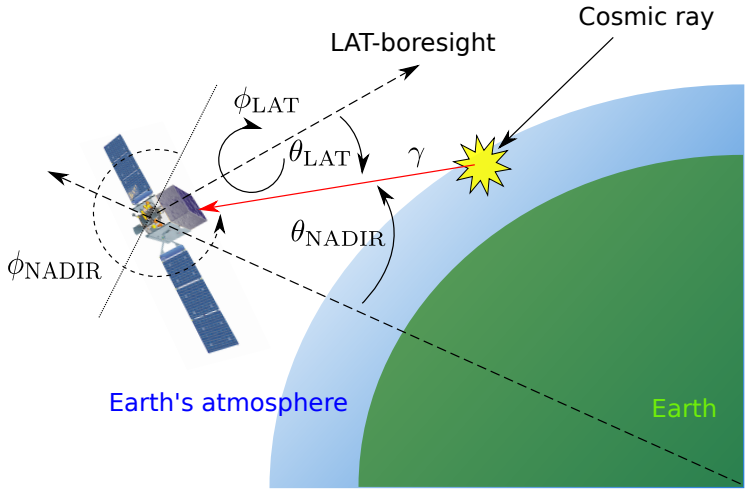

Figure 4.1: Schematics of the Earth's γ-ray production from CR interaction with the upper atmosphere.

Figure 4.1 demonstrates the definitions of some important angular variables describing a photon's direction in this analysis. The nadir angle ($\theta_{\rm NADIR}$) is the angle between a photon's and the nadir direction. The incidence angle ($\theta_{\rm LAT}$) is the angle of a photon's direction with respect to the detector's boresight. The angle $\phi_{\rm LAT}$ specifies the azimuthal angle of a photon in the LAT's reference frame.

4.1 Data selection

In this work, 9 years of LAT's photon and spacecraft data have been used. We use the latest version of event reconstruction (Pass 8) with the cleanest photon event class[1] (ULTRACLEANVETO) in this work. All data sets can be downloaded pubically from the LAT's database website[2].

To select the Earth's limb photon produced in the thin-target regime where the absorption effect could be neglected, we follow the same criteria ($68.4^\circ < \theta_{\rm NADIR} < 70.0^\circ$) used in the previous LAT analysis by Ackermann et al. (2014). We select photons between 10 GeV and 1 TeV which would be correspond to the CR proton rigidity range of roughly 60 GV to 2 TV (Ackermann et al. 2014). We also cut photons with $\theta_{\rm LAT} > 70^\circ$ to avoid mis-reconstructions of highly off-axis photons.

4.2 Flux extraction

The definition of the Earth's limb flux in the energy bin i is given by

$$\textbf{Flux}(E_i) = \frac{dN}{dE}(E_i) = \left(\sum_{\rm pixel} \frac{\rm Count_i}{\rm Exposure_i} \right) \frac{1}{\Delta\Omega\Delta E} \tag{4.1}$$

where $\rm Count_i$ is the photon count, $\rm Exposure_i$ is the exposure, $\Delta\Omega$ is the solid angle size of the limb region, and ΔE is the energy bin width. Since the CR spectrum follows a power law in the energy range of this analysis, we expect a power law in the Earth's γ-ray emission spectrum. Therefore, to calculate the Earth's γ-ray spectrum, we divide the energy into 50 bins equally spaced in log scale from 10 GeV to 1.0 TeV.

The flux calculation procedure can be summarized in the following steps.

1. Analyze 50 bins in energy between 10 GeV - 1 TeV with equal logarithmic spacing

[1] https://fermi.gsfc.nasa.gov/ssc/data/analysis/documentation/Cicerone/Cicerone_Data/LAT_DP.html

[2] https://fermi.gsfc.nasa.gov/ssc/data/access/lat

2. Create 2D histogram count maps from photon data for each energy bin

3. Create 2D histogram exposure maps (effective area × livetime) from spacecraft data for each energy bin

4. Calculate the Earth's γ-ray flux using the count and exposure maps by Equation 4.1

5. Perform background subtraction from an average background distribution (Define background in range $72.0^\circ < \theta_{\mathrm{NADIR}} < 80.0^\circ$)

4.2.1 Exposure map calculation

The exposure map calculation is the most complicated step in this work because we have to perform coordinate transformation. In the standard spacecraft data files, the LAT positions and orientations are recorded in equatorial coordinates. We have to make a coordinate transformation to obtain the position of any given pixel in an exposure map in the spacecraft's reference frame in order to derive the corresponding effective area for that pixel.

Coordinate transformations

Spacecraft's position and orientation (direction of the LAT's boresight and solar panel) are recorded in the equatorial coordinates for which we denote with a symbol "eq". We can define the Cartesian axes for the equatorial coordinate by letting the x-axis ($\hat{x}_{\mathrm{eq}}$) point to the vernal equinox for which the right ascension (RA) is 0° and letting the z-axis point to the pole for which the declination (DEC) is 90°.

We analyze the Earth's γ-ray emission in the local-zenith coordinate system denoted by the symbol "zn," as viewed locally by the LAT. Here we define that $\hat{x}_{\mathrm{zn}}$ points along the local zenith direction of the LAT, and that $\hat{z}_{\mathrm{zn}}$ points perpendicular to $\hat{x}_{\mathrm{zn}}$ in the $\hat{x}_{\mathrm{zn}}$-$\hat{z}_{\mathrm{eq}}$ plane. The "eq" and "zn" coordinate systems are illustrated in Figure 4.2. Here we assume that $\hat{x}_{\mathrm{zn}}$ makes an angle δ_{zn} with the

$\hat{x}_{\rm eq}$ and $\hat{y}_{\rm eq}$ plane, and $\alpha_{\rm zn}$ is the azimuthal angle of $\hat{x}_{\rm zn}$ projection onto the $\hat{x}_{\rm eq}$ and $\hat{y}_{\rm eq}$ plane.

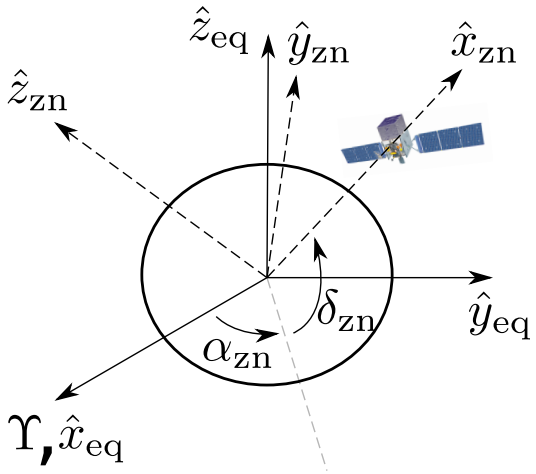

Figure 4.2: Illustration of the relationship between the equatorial (eq) and local-zenith (zn) coordinate systems for the LAT.

We can write the components of the zn system in terms of the eq system as

$$\begin{aligned}
\hat{x}_{\rm zn} &= \cos\delta_{\rm zn}\cos\alpha_{\rm zn}\hat{x}_{\rm eq} + \cos\delta_{\rm zn}\sin\alpha_{\rm zn}\hat{y}_{\rm eq} + \sin\delta_{\rm zn}\hat{z}_{\rm eq} \\
\hat{z}_{\rm zn} &= -\sin\delta_{\rm zn}\cos\alpha_{\rm zn}\hat{x}_{\rm eq} - \sin\delta_{\rm zn}\sin\alpha_{\rm zn}\hat{y}_{\rm eq} + \cos\delta_{\rm zn}\hat{z}_{\rm eq} \\
\hat{y}_{\rm zn} &= \hat{z}_{\rm zn} \times \hat{x}_{\rm zn}.
\end{aligned} \tag{4.2}$$

Equation 4.2 can be written more compactly in a matrix form with

$$\hat{r}_{\rm zn} \equiv T_{\rm eq\to zn}(\delta_{\rm zn}, \alpha_{\rm zn})\hat{r}_{\rm eq}, \tag{4.3}$$

where $T_{\rm eq\to zn}$ is the transformation matrix which depends on the values of $\delta_{\rm zn}$ and $\alpha_{\rm zn}$.

Two variables for determining the LAT boresight orientation are described in equatorial coordinates as declination angle ($\delta_{\rm p}$) and the right ascension angle ($\alpha_{\rm p}$). A full representation of the zn and sp coordinates could be written as Equation 4.4. The compact form is in Equation 4.5.

$$\begin{aligned}
\hat{x}_{\rm p} &= \cos\delta^{\rm x}_{\rm p}\cos\alpha^{\rm x}_{\rm p}\hat{x}_{\rm eq} + \cos\delta^{\rm x}_{\rm p}\sin\alpha^{\rm x}_{\rm p}\hat{y}_{\rm eq} + \sin\delta^{\rm x}_{\rm zn}\hat{z}_{\rm eq} \\
\hat{z}_{\rm p} &= \cos\delta^{\rm z}_{\rm p}\cos\alpha^{\rm z}_{\rm p}\hat{x}_{\rm eq} + \cos\delta^{\rm z}_{\rm p}\sin\alpha^{\rm z}_{\rm p}\hat{y}_{\rm eq} + \sin\delta^{\rm z}_{\rm zn}\hat{z}_{\rm eq} \\
\hat{y}_{\rm p} &= \hat{z}_{\rm p}\times\hat{x}_{\rm p}
\end{aligned} \tag{4.4}$$

$$\hat{r}_{\rm p} \equiv T_{\rm eq\to p}(\delta^{\rm x}_{\rm p}, \alpha^{\rm x}_{\rm p}, \delta^{\rm z}_{\rm p}, \alpha^{\rm z}_{\rm p})\hat{r}_{\rm eq} \tag{4.5}$$

Similarly, $T_{\rm eq\to p}$ is also considered as a transformation matrix.

The LAT coordinate system is defined such that $\hat{z}_{\rm p}$ points along the boresight and $\hat{x}_{\rm p}$ points along with one of its solar panels. The directions of $\hat{x}_{\rm p}$ and $\hat{z}_{\rm p}$ are also recorded in the equatorial system. Figure 4.3 shows the relationship between the sp and zn coordinate systems.

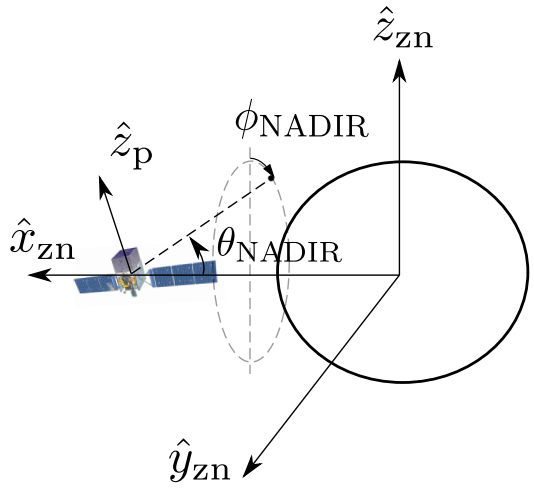

Figure 4.3: Illustration of the local zenith (zn) and the plane of detector (p) coordinate systems. The nadir ($\theta_{\rm NADIR}$) and azimuthal ($\phi_{\rm NADIR}$) angles of a pixel of interest are also shown.

With the two transformation matrices, $T_{\rm eq\to zn}$ and $T_{\rm zn\to p}$, we can transform the position of a pixel in a local zenith coordinate map into the LAT coordinate system to obtain the effective area for that pixel. The exposure for that pixel is the sum of effective are $\times$ lifetime. The spacecraft coordinate can be written as a dependency of Earth's polar coordinate as Equation 4.2.1 in the cartesian system.

$$\hat{r}_{\rm zn}(\theta_{\rm NADIR}, \phi_{\rm NADIR}) \equiv -\cos\theta_{\rm NADIR}\hat{x}_{\rm zn} + \sin\theta_{\rm NADIR}\sin\phi_{\rm NADIR}\hat{y}_{\rm zn} + \sin\theta_{\rm NADIR}\cos\phi_{\rm NADIR}\hat{z}_{\rm zn}$$

Extracting the relations to simplify the LAT's boresight coordinate could be contained by one inversion of transformation matrix from equatorial to spacecraft and transform it to plane of the detector as written in the compact form in Equation 4.6.

$$\hat{r}_{\rm p}(\theta_{\rm N}, \phi_{\rm N}) = T_{\rm eq\to p}(\delta^{\rm x}_{\rm p}, \alpha^{\rm x}_{\rm p}, \delta^{\rm z}_{\rm p}, \alpha^{\rm z}_{\rm p})\left[T_{\rm eq\to zn}(\delta_{\rm zn}, \alpha_{\rm zn})\right]^{-1}\hat{r}_{\rm zn}(\theta_{\rm NADIR}, \phi_{\rm NADIR}) \quad (4.6)$$

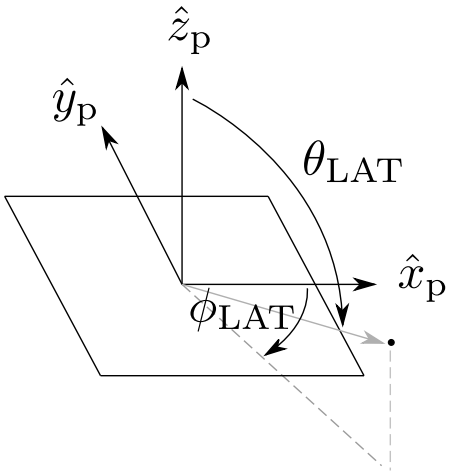

Figure 4.4: A vector pointing to a pixel of interest (grey arrow) in the plane of detector (p) coordinates. The $\hat{z}_{\rm p}$ axis points along the LAT's boresight and the $\hat{x}_{\rm p}$ axis points along with one of its solar panels.

Geometrically, an angular coordinate of the LAT plane could be obtained from a normalized component of the cartesian unit vector as in Figure 4.4. The exposure accumulation has been calculated in every single grid from the previous relation.

Parallel computations

The complexity of the code becomes large due to the transformation operation. For example, a plain matrix inversion cost $\mathcal{O}(n^3)$ where n is 3 because

it is a 3 by 3 matrix in this case. The matrix multiplication also costs the same amount of complexity, rendering exposure map calculation a very computationally intensive task.

The spacecraft files, which contain the information of the LAT position, orientation, and status in rows of the 30-second time step, are called the FT2 files. We use 25 energy bins per decade, so the bin width is small enough to use the geometric mean to represent the mean energy for each bin. Moreover, the exposure maps can be calculated separately for a given time period. We can therefore split the 9-year analysis time into many small time periods, calculate the exposure maps for each time period in parallel, and sum all periods to obtain the total exposure maps.

The code is implemented in Message Passing Interface (MPI). The framework provides a simple protocol for communication between each process with a customizable message schema. It assists the user to freely control multiple processes with full control of each process. According to Flynn's taxonomy of computation, this work exploits the Multiple Instruction Multiple Data (MIMD) architecture to utilize the resources in a distributed system.

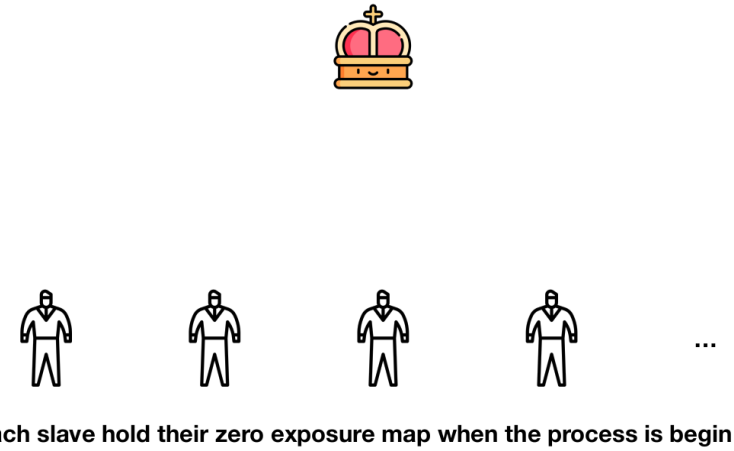

Figure 4.5: Spawning the king and slave processes

In the normal parallel computing setup, sending equal amount of task to each node is not optimized since there would be fast and slow nodes with different performances. Some trivial tasks can lock resources in a computing cluster and

blocks the resource allocation for other tasks. To maximize the usage of the CPU-based cluster computing, there is a mechanism called the "Master-Slave technique". The algorithm has been designed for utilizing the resource by spawning a king as the process manager and multiple slaves to be process workers. The starting process could be demonstrated in Figure 4.5.

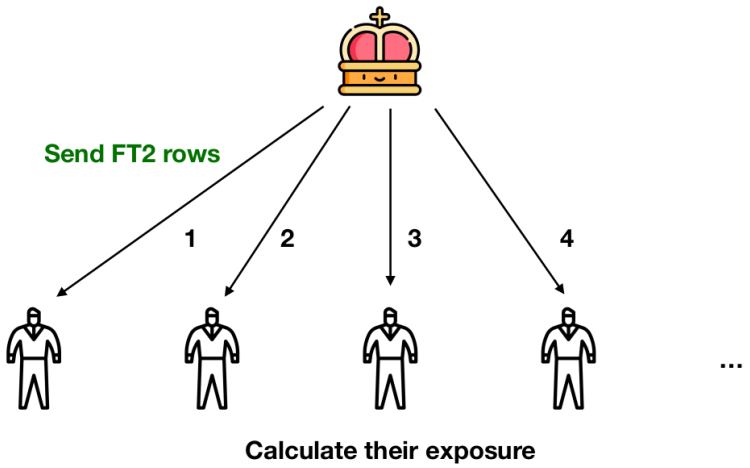

Figure 4.6: Master process sends a small task to slaves.

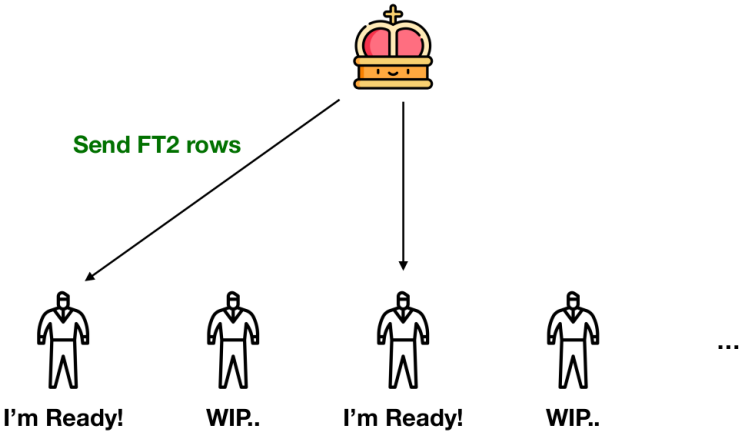

Figure 4.7: Asynchronous assignment of tasks to available slaves.

A certain amount of spacecraft information (FT2 rows) would be sent as an input to slaves sequentially until all slaves are assigned with a small task and start the calculation. There are metadata attached to the message. One of the options is the status tag which let the slaves declare the status of a process

whether it is still in process or has finished. Figure 4.7 illustrates the non-sequential assignment of the workload. Small tasks are sent to available slaves and skip busy slaves. This mechanism allows the execution to utilize the resource in a cluster without wasting free slaves. After all tasks are assigned, the master process will send a status tag announcing that the overall calculation has finished. Then, the exposure maps from all slaves would be added to obtain the final total exposure maps. The benchmark for the calculation time of serial code and parallel code is reported in Appendix A.

4.3 Hadronic collision model

CR spectrum is well described by power in ridigity where the ridigity is the momentum per charge of a particle. The explicit formula for a single power-law (SPL) spectrum in rigidity for proton is shown in Equation 4.7 where Γ represents the spectral index of the model. Converting between the ridigity (R) and the energy spectrum is derived in Appendix B.

Single power law (SPL)

$$\frac{dN}{dR} = N_0 R^{-\Gamma} \tag{4.7}$$

where N_0 is the normalization of the power law. The most crucial part of this work is to determine if there is any breaking in the spectral index of the power law. To represent single breaking energy, a broken power law (BPL) could be modeled by Equation 4.8.

Broken power law (BPL)

$$\frac{dN}{dR} = \begin{cases} N_0 R^{-\Gamma_1} & : \ E < E_{\text{Break}} \\ N_0 [R(E_{\text{Break}})]^{\Gamma_2 - \Gamma_1} R^{-\Gamma_2} & : \ E \geq E_{\text{Break}} \end{cases} \tag{4.8}$$

The collision of incoming CR protons with kinetic energy above 10 GeV striking the Earth's atmosphere can be modeled by thin-target proton-proton interactions for which the normalization depends on the chemical composition and density of the air. The proton-proton collision yielding γ rays as secondary products

for a broad and smooth spectrum of proton can be modeled by Equation 4.9 taken from Kachelrieß & Ostapchenko (2012) as

$$\frac{dN_\gamma}{dE_\gamma} \propto \int_{E_\gamma}^{E_{\max}} dE' \frac{dN_p}{dE'} \frac{d\sigma^{pp\to\gamma}}{dE_\gamma}(E', E_\gamma), \tag{4.9}$$

where $d\sigma^{pp\to\gamma}(E', E_\gamma)/dE_\gamma$ contains the scattering amplitude for the kinetic energy of proton (E') and the energy of γ-ray (E_γ). Atmospheric components consists of 78% nitrogen and 21% oxigen (Wallace & Hobbs 2006). The relation of the proton-proton and proton-air scattering amplitudes is obtained from Atwater & Freier (1986a) which depends on the atomic numbers of the air molecules.

The second highest fraction of the arrival CR particles on Earth is an alpha (α) particle. particle (the nucleus of a helium atom) for which the contribution to the secondary γ-ray products is not negligible. We use $\sigma_{\alpha N}/\sigma_{pN} \approx 1.6$ in the energy range of this analysis from the hadronic cascade cross-section approximation (Atwater & Freier 1986a). Hence, the γ-ray spectrum produced from CR proton and α scattering with air molecules can be described by

$$\frac{dN_\gamma}{dE_\gamma}(E_\gamma) \propto \sum_{E_i'} \left[\frac{E_i'}{E_\gamma}\Delta(\ln E_i')\right] \left[f_{pp}\frac{dN_p}{dE_i'}\left\{1 + \frac{\sigma_{\alpha\mathrm{N}}}{\sigma_{p\mathrm{N}}}\left(\frac{dN_p}{dR}\right)^{-1}\frac{dN_\alpha}{dR}\frac{dR_\alpha}{dR_p}\right\}\right], \tag{4.10}$$

where f_{pp} is the proton-proton to γ cross section taken from Kachelrieß & Ostapchenko (2012). The CR α spectrum (dN_α/dR) would not be measured in this work since there will be multiple parameters that lead to an overwhelming local optimum. We therefore fix the α spectrum to that measured by Aguilar et al. (2015) and optimize only the proton spectral parameters. The full detail of the equation derivation is demonstrated in the Appendix D.

4.4 Optimization

Determining the best-fit spectral model requires an objectives function to represent how well the model match with the observed data. A proper optimization algorithm is a crucial part since it is likely that the local optima exist in the

parameters space. A poor optimization could lead the best-fit stuck in a local minimum and yield a poor result. To avoid local optima, heuristic optimization is employed for finding the global best-fit of the model in parameter space.

Poisson likelihood function

An objective function is defined as the logarithmic of Poisson likelihood function in Equation 4.11 because we would like to evaluate the Poisson probability (P_{pois}) that we observe $n_{\text{i,measurement}}$ photons if the model yields $n_{\text{i,model}}$ photons for the i^{th} bin of N energy bins. Converting a spectral model into a count histogram is simply multiplying the model flux and the exposure in the limb region. We can then calculate the likelihood of a given model by

$$\text{log-likelihood} = -\sum_{i=1}^{N} \log P_{\text{pois}}(n_{\text{i,model}}, n_{\text{i,measurement}}) \tag{4.11}$$

The negative sign is included in the definition of the log likelihood function to make the numerical algorithm more convenient by requiring minimization rather than maximization of the objective function.

Particle Swarm Optimization (PSO)

In the early phase of the analysis, the plain gradient descent optimization was used for model fitting. The result turned out that different initial parameters yielded different best-fit model which implied the local minima in the problem. There is no method to guarantee the global minimum but the heuristic optimization could be a better option for handling this type of problem. One kind of most widely used algorithm is particle swarm optimization (PSO) invented by Kennedy & Eberhart (1995).

In order to get the best-fit CR spectral model, we employ the PSO by randomly initiating many particles in a given range of the parameter space and finding the sets of parameters which represent the local and global best fit in a given step of the iteration. In the next iteration, we slowly move those particles toward to the local and global position in parameter space with a proper weight. The

iteration process will stop when the standard deviation of the objective function from every particle is less than a certain threshold. The explicit formula for every k iteration which moves particle i with velocity v_k^i is

$$v_{k+1}^i = \omega v_k^i + c^b r_k^b [b_k^i - x_k^i] + c^B r_k^B [B_k^i - x_k^i], \tag{4.12}$$

and we update the position of particle i (x_k^i) in the parameter space with

$$x_{k+1}^i = x_k^i + v_{k+1}^i. \tag{4.13}$$

where b and B are best local and global parameter sets along the optimization process and set $\omega = 0.2$, $c^b = 0.2$ and $c^B = 0.3$.

4.5 Statistical significance

Models with a larger number of parameters or complexity certainly yield better performance except that they overfit the problem. The critical issue is to answer how significant such alternative model could outperform the null-hypothesis model.

In this work, the BPL model has 2 more degrees of freedom (DOF) than the SPL model does and always result in a better fit than the SPL does.

To compare the null (SPL) and alternative (BPL) hypothesis, we use the one-tail testing taken into account the difference in DOF as adopted by adopted by Huelsenbeck & Crandall (1997). This method called "Likelihood ratio test (LRT)". The compact formula is

$$\mathrm{LRT} = -2 \ln \left(\frac{\mathcal{L}_{\mathrm{null}}}{\mathcal{L}_{\mathrm{alternative}}} \right). \tag{4.14}$$

CHAPTER V
RESULTS AND DISCUSSION

This chapter reports the detail of the analysis procedures which include the data correction process, count maps from the raw count, exposure map from the parallel computation, the spectrum calculation, and inversive fitting of the spectral models from heuristic optimization.

5.1 Limb angle correction

From the observations, the peak of the Earth's limb γ-ray θ_{NADIR} profile changes over time since the spacecraft altitude is gradually getting lower each year, effectively increasing the peak position of θ_{NADIR} from the LAT's point of view.

The top-left of Figure 5.1 demonstrates how spacecraft orbiting altitude affects the θ_{NADIR} profile by showing a 2D histogram of photon count in each altitude and θ_{NADIR} bin. The bottom-left plot is the projection of the previous raw count 2-D histogram onto the θ_{NADIR} axis which shows a peak around 68°. Both bottom and top right histograms are constructed in a similar idea but with the spacecraft altitude correction on the θ_{NADIR} which reduce the effect of the LAT orbital decay over time. The region of interest used to calculate the Earth's limb γ-ray spectrum is highlighted in orange, and the region highlighted in blue gives an estimate of the background photons which is subtracted from the limb flux. Note that the Earth's limb emission is approximately one order of magnitude brighter than the background emission.

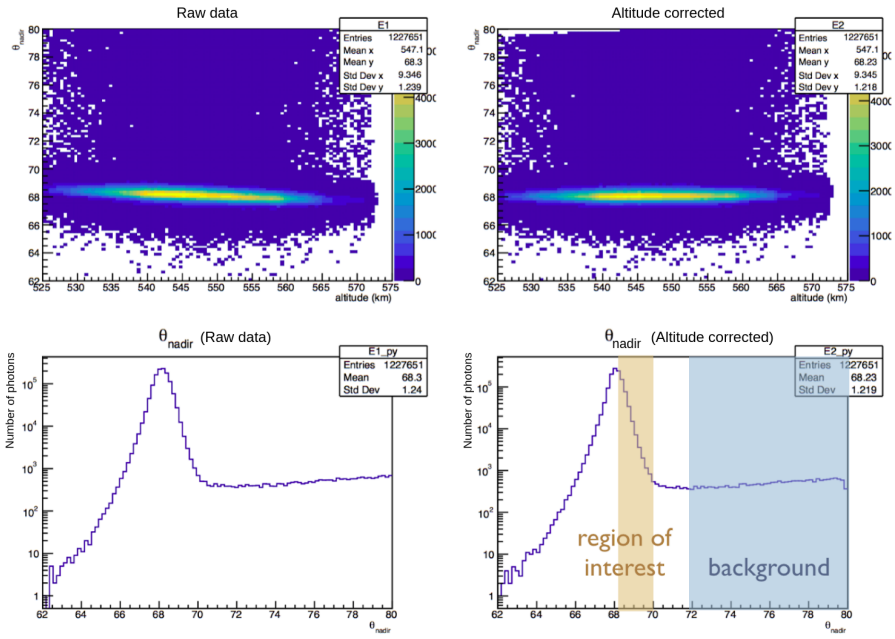

Figure 5.1: Distribution of number of photons above 20 MeV with nadir angle (θ_{NADIR}) before (left) and after (right) altitude correction. Top panels show 2D histograms of number of photons in each θ_{NADIR} and altitude (in km) bin. Bottom panels show the projection of the 2D histograms in the top panels onto the θ_{NADIR} axis in which photons from all altitudes are accumulated into each θ_{NADIR} bin.

5.2 Earth's limb γ-ray spectrum measurement

According to Equation 4.1, the first step is the construction of count maps in the local zenith coordinates. Visualization of a raw count map above 10 GeV from 1 week of data is demonstrated in Figure 5.2.

The limb's region could be easily observed in the bright ring at $\theta_{\mathrm{NADIR}} \approx 68°$. Figure 5.2 shows more brightness from the north and south limb due to the LAT's survey mode configuration which results in higher exposure in the north and south regions. Projection of the 2D histogram in Figure 5.2a onto a 1D histograms of the azimuthal angle (ϕ_{NADIR}) is shown in Figure 5.2b which roughly illustrates the East-West effect (more photons from the West) although the exposure has not been taken into account yet. The asymmetric distribution could caused from the asymmetric exposure which will be investigated later in this section. To illustrate the East-West effect in γ-ray, projecting the photon intensity into ϕ_{NADIR} axis is visualized in Figure 5.3.

Figure 5.4 shows the count maps in 4 energy bands (as examples from

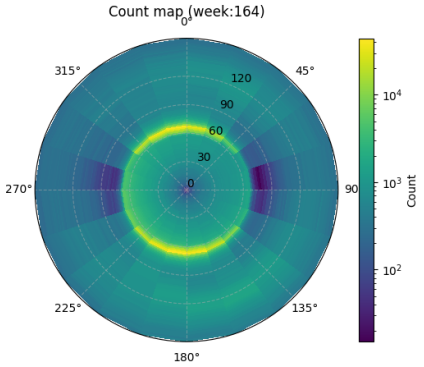

(a) 2D histogram of ¿10 GeV photons binned in nadir angle (θ_{NADIR}) along the radial direction and azimuthal angle (ϕ_{NADIR}) along the azimuthal direction.

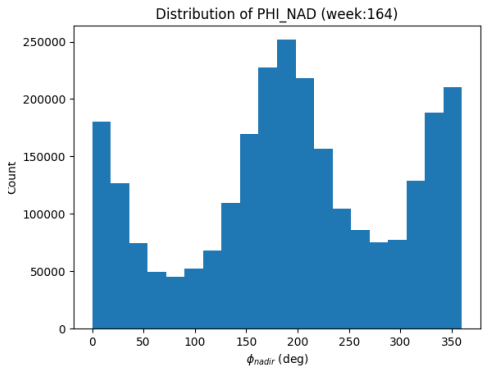

(b) Distribution of photon counts with ϕ_{NADIR} for $0° < \theta_{\mathrm{NADIR}} < 150°$.

Figure 5.2: An example distribution of γ rays above 10 GeV from 1 week of LAT data

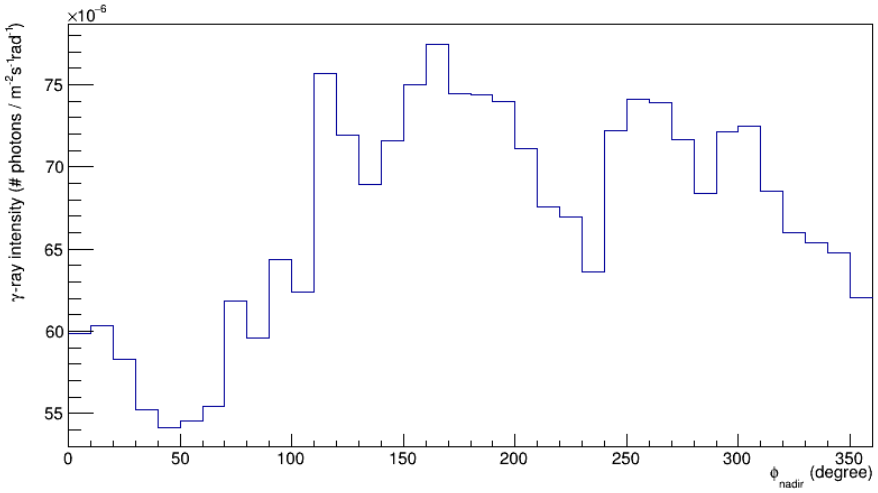

Figure 5.3: Earth's γ-ray intensity in ϕ_{NADIR} axis

50 bands total) in the local zenith coordinate system where the Earth is placed at the center of each map. The limb emission can be seen clearly as shiny thin rings which become dimmer at higher energy.

The next step is the exposure calculation. The exposure map is computed by accumulating exposure time from the LAT's FoV in each time step as well as takes in to account the detector efficiency as a function of incident angle and energy. Examples of exposure maps, for which the unit is area $\times$ time, are shown in Figure ??.

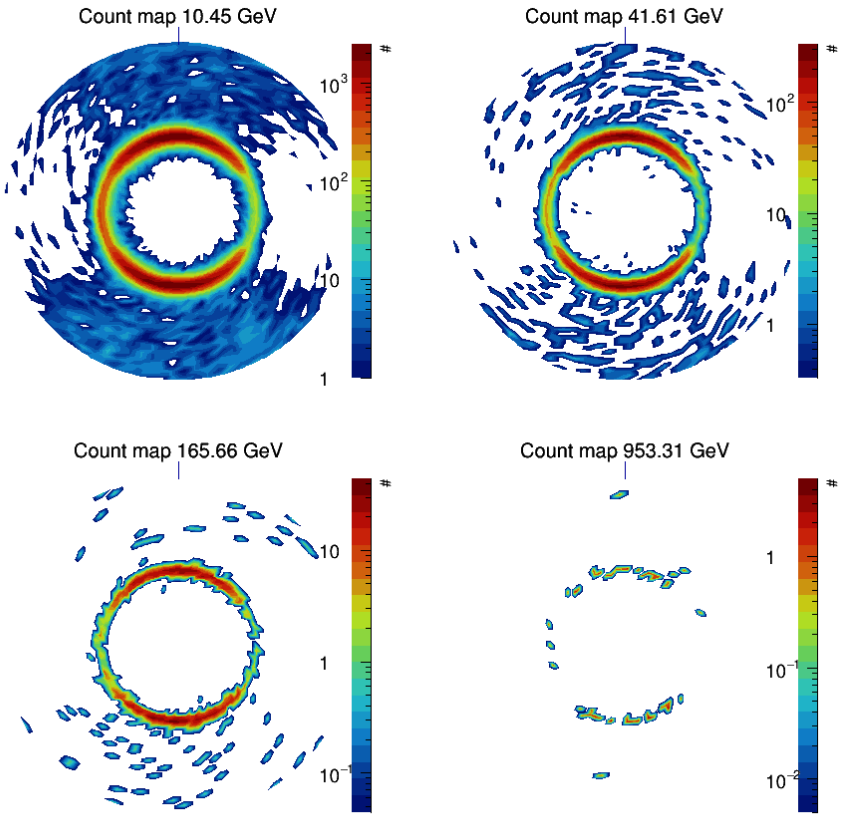

Figure 5.4: Count maps in the local zenith coordinates. The bright emission ring is located at the limb ($\theta_{\mathrm{NADIR}} \approx 68°$). The radial axis is in range $60° < \theta_{\mathrm{NADIR}} < 80°$ and the clockwise direction is starting from $\phi_{\mathrm{NADIR}} = 0°$ to $\phi_{\mathrm{NADIR}} = 360°$.

Examples of exposure maps in local-zenith coordinates are shown in Figure 5.5, indicating that the sky exposure (region near the edge of the each plot) is an order of magnitude higher than that for the Earth because the LAT is configured to survey the sky and avoid pointing directly at Earth. Regarding the exposure of the Earth's limb region ($\theta_{\mathrm{NADIR}} \approx 68°$), the north and south exposure is higher than that for the east and west because of the LAT's survey configuration which switches between pointing north and south of its orbital plane every orbit. The exposure of the western limb is slightly higher than that of the eastern limb.

To obtain flux maps, we divide the count by the exposure maps bin by bin. We integrate the flux map in the limb region ($68.4° < \theta_{\mathrm{NADIR}} < 70.0°$) and divide by the energy bin width and the solid angle size of the region to obtain a spectral value for that energy bin. After repeating the calculation for 50 energy

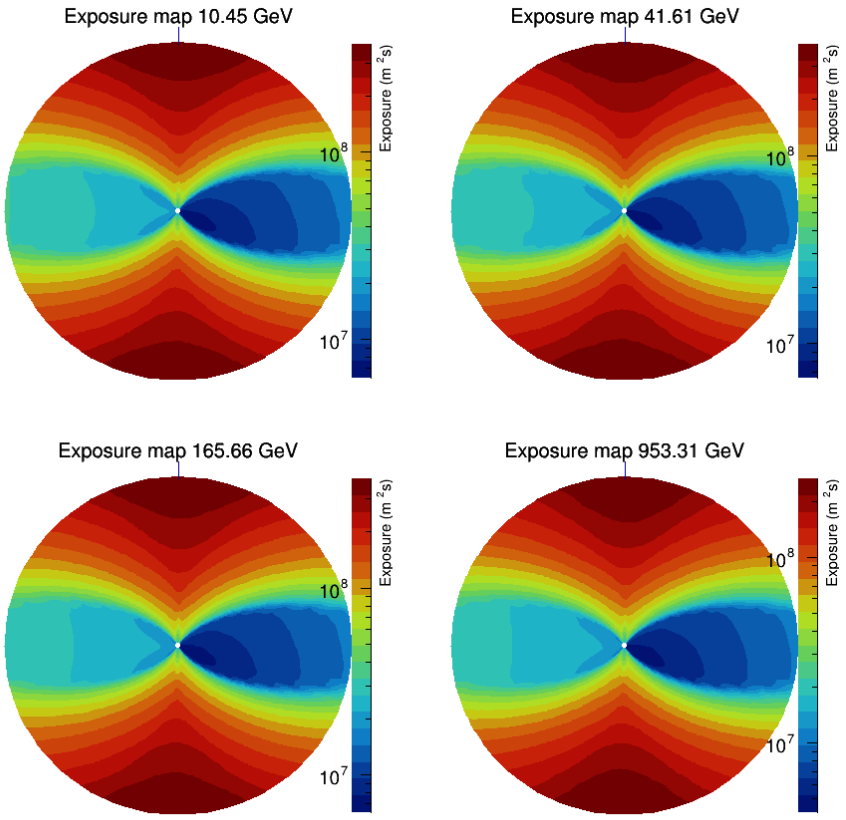

Figure 5.5: Exposure maps in local-zenith coordinates in 4 energy bands. The Earth's limb is indicated by the dotted circle in which the north, east, south, and west part of the limb are labeled.

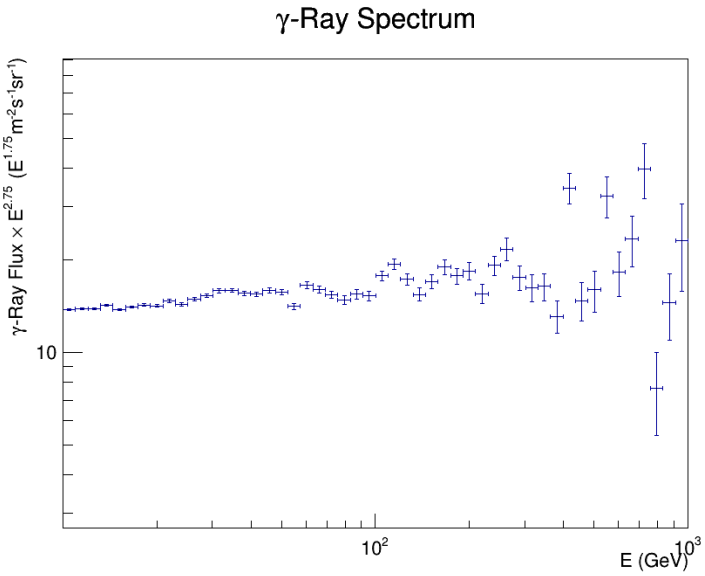

Figure 5.6: Measured Earth's limb γ-ray spectrum from $68.4° < \theta_{\mathrm{NADIR}} < 70.0°$ by this work.

bins and subtracting the background flux from the sky (see Figure 5.1), we have the final Earth's γ-ray spectrum as illustrated in Figure 5.6.

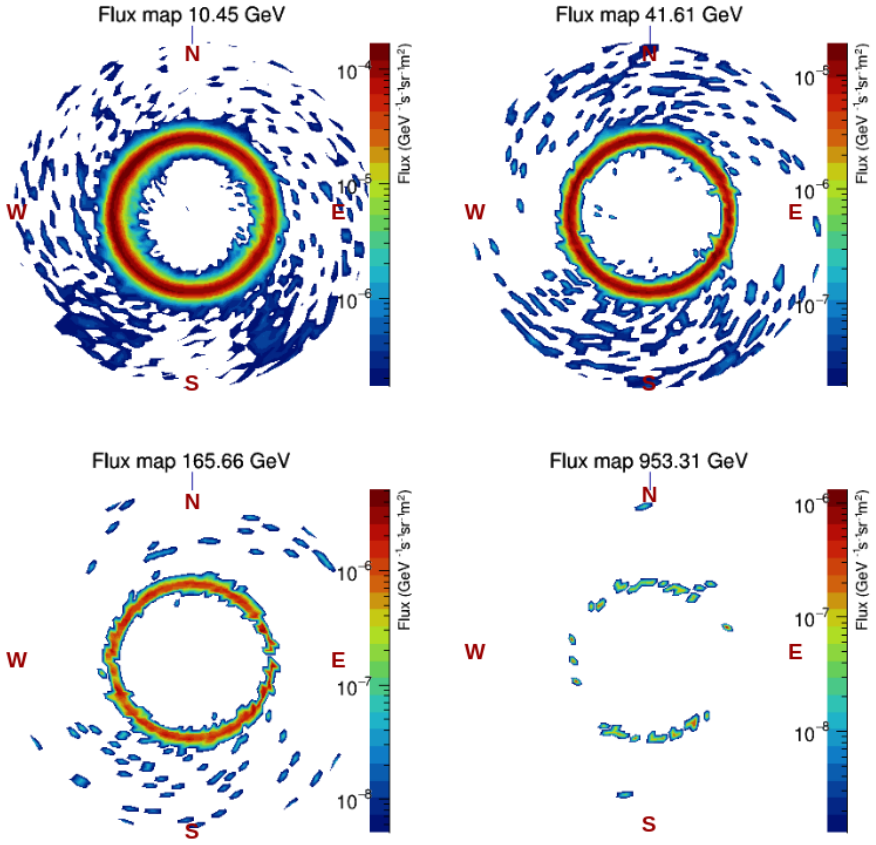

Figure 5.7: Flux maps of of the Earth's γ-ray emission in local zenith coordinates where the Earth is at the center of each panel and the ring is the γ-ray emission from the limb.

Examples of γ-ray flux maps in local zenith coordinates are visualized in Figure 5.7, clearly showing the bright ring-like emission from the Earth's limb. The East-West effect can be observed from the thicker emission region and brighter flux from the west limb. It means that not only is the intesity brighter but also the ring thickness of the limb region is larger from the west compared to those from the east.

As it can be seen that the expsoure maps where the north and south is much higher than the east and west which caused from the orbit orientation of the spacecraft. It is suspected that the measured γ-ray spectrum might not a robust results from some vanishing area in the calculation. The above clue leads this work

to perform another parallel study where the γ-ray from the Earth's limb takes only north and south direction into account. The study in Appendix F was done by applying filter ϕ_{NADIR} from 330°to 30 °as well as between 150°and 210°.

5.3 Best fit results

The optimized parameters for Single Power Law (SPL) and Broken Power Law (BPL) models are summarized in Table 5.1. Best fit γ-ray spectra from both models are visualized in Figure 5.8 along with the Earth's γ-ray spectrum from the measurement. Our best fit BPL result is consistent with direct measurements by AMS-02 (Aguilar et al. 2015) and PAMELA (Adriani et al. 2011) which identify the CR proton spectral breaking at 300 GeV as qualitatively illustrated in Figure 5.9. Our results are also consistent with the indirect measurement by the LAT Ackermann et al. (2014) which reported the best-fit BPL spectral indices of $\Gamma_1 \approx 2.81$, $\Gamma_2 \approx 2.61$, and the break energy at 302 GeV.

Best fits	Γ_1	Γ_2	E_{Break} (GeV)
SPL	2.70 ± 0.08 (0.06)	-	-
BPL	2.86 ± 0.14 (0.08)	2.63 ± 0.13 (0.10)	333 ± 10 (9)

Table 5.1: Optimized parameters for the SPL and BPL models for CR protons from this work where Γ_1 and Γ_2 are spectral indices below and above the break energy (E_{Break}), respectively. Reportoed deviation is reported in total error and the following bracket is a statistical error. The description for error estimation can be found in Appendix E.

However, a more complex model would perform better than a simpler model with less degrees of freedom. Determining the statistical significance would be a quantitative method to assess if the BPL model fits the data better than the SPL model does. The significance level is evaluated by the likelihood ratio test based on the likelihood (Equation 4.14) of the null hypothesis (SPL) and the likelihood of the alternative hypothesis (BPL) taking into account the difference in the degrees of freedom between the two models. We find that the BPL fits the measurement better than the SPL does by around 1.38σ or at 92% confidence level.

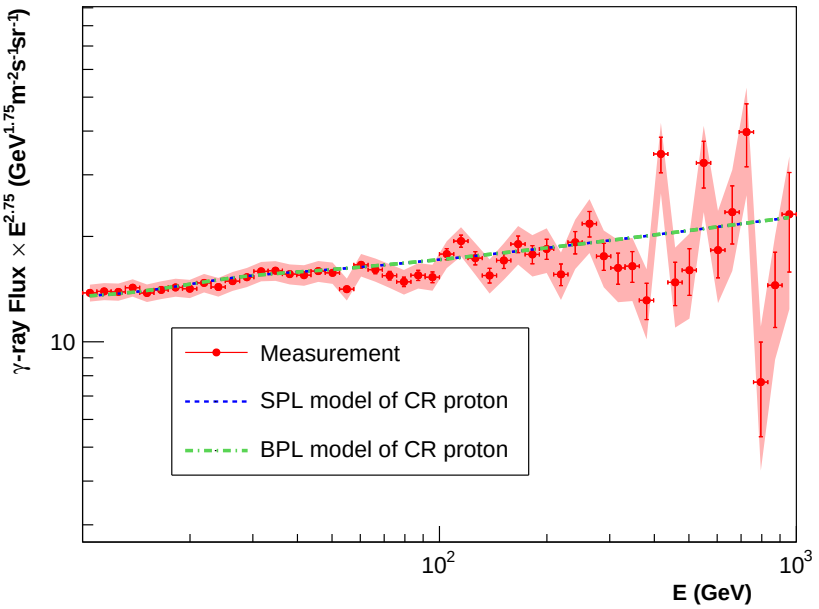

Figure 5.8: The Earth's γ-ray spectra calculated from the SPL (blue) and BPL (green) models of CR proton which best fit to the measured spectrum in the thin-target regime (red).

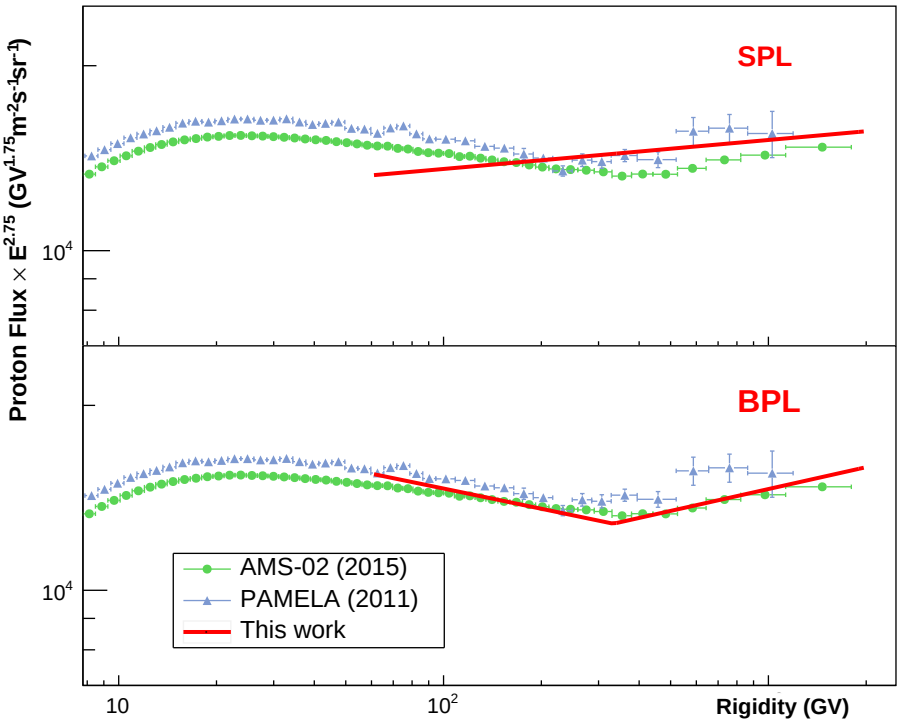

Figure 5.9: Best-fit CR proton spectra from this work (red) compared to the direct measurements by AMS-02 (blue) and PAMELA (green).

CHAPTER VI
CONCLUSION

In this study, we indirectly measure the CR proton spectrum between 60 GeV – 2 TeV using the Earth's γ-ray spectrum with the LAT data. We construct the Earth's γ-ray spectrum by analyzing the photon count and the LAT exposure above 10 GeV in the local zenith coordinates from 9 years of data (Aug 2008 to Oct 2017). We use photons of the cleanest event class (P8UltracleanVeto) which are produced by the interactions of CRs and the Earth's upper atmosphere in the thin-target regime ($68.4^\circ < \theta_{\rm NADIR} < 70.0^\circ$). An indirect measurement of the proton spectrum is inversely computed via the $pp \to \gamma$ interaction model with a heuristic optimization technique.

Our best-fit single power law (SPL) model for CR proton yields the spectral index value of 2.70 ± 0.08, while the best-fit broken power law (BPL) model yields a hardening of CR proton from the spectral index of 2.86 ± 0.14 to 2.63 ± 0.13 at 333 ± 10 GeV. The BPL model fits the data better than the SPL model does at the statistical significance of 1.38σ, corresponding 92% confidence level which according to standard convention is not strong enough to conclusively declare the spectral break from this analysis alone. Nevertheless, we confirm the best-fit models and improve the significance level from 1.0σ in the previous study by the LAT. Although precision measurement by AMS-02 and other direct measurements have settled the existence of this CR proton spectral break at approximately 340 GV, having independent supports from different experiments such as this work is valuable. Spectral features will help us understand the origins and propagation of Galactic CRs in the future.

REFERENCES

1. Abdo, A. A., Ackermann, M., Ajello, M., Atwood, W. B., Baldini, L., Ballet, J., et al. (2009). Fermi large area telescope observations of the cosmic-ray induced γ-ray emission of the earth's atmosphere. *Phys. Rev. D*, 80, 122004.
2. Abdo, A. A., Ackermann, M., Ajello, M., Atwood, W. B., Baldini, L., Ballet, J., et al. (2009). Fermi large area telescope observations of the cosmic-ray induced γ-ray emission of the Earth's atmosphere. *Physical Review D*, 80(12), 122004.
3. Abraham, J., Abreu, P., Aglietta, M., Ahn, E., Allard, D., Allen, J., et al. (2010). Measurement of the energy spectrum of cosmic rays above 1018 ev using the pierre auger observatory. *Physics Letters B*, 685(4-5), 239–246.
4. Ackermann, M., Ajello, M., Albert, A., Allafort, A., Baldini, L., Barbiellini, G., et al. (2014). Inferred Cosmic-Ray Spectrum from Fermi Large Area Telescope γ-Ray Observations of Earth's Limb. *Physical Review Letters*, 112(15), 151103.
5. Ackermann, M., Ajello, M., Allafort, A., Atwood, W. B., Baldini, L., Barbiellini, G., et al. (2012). Measurement of Separate Cosmic-Ray Electron and Positron Spectra with the Fermi Large Area Telescope. *Physical Review Letters*, 108(1), 011103.
6. Adriani, O., Barbarino, G., Bazilevskaya, G., Bellotti, R., Boezio, M., Bogomolov, E., et al. (2009). An anomalous positron abundance in cosmic rays with energies 1.5–100 gev. *Nature*, 458(7238), 607–609.
7. Adriani, O., Barbarino, G., Bazilevskaya, G., Bellotti, R., Boezio, M., Bogomolov, E., et al. (2011). Pamela measurements of cosmic-ray proton and helium spectra. *Science*, 332(6025), 69–72.
8. Aguilar, M., Aisa, D., Alpat, B., Alvino, A., Ambrosi, G., Andeen, K., et al.

(2015). Precision Measurement of the Helium Flux in Primary Cosmic Rays of Rigidities 1.9 GV to 3 TV with the Alpha Magnetic Spectrometer on the International Space Station. *Physical Review Letters*, 115(21), 211101.

9. Aguilar, M., Aisa, D., Alpat, B., Alvino, A., Ambrosi, G., Andeen, K., et al. (2015). Precision measurement of the helium flux in primary cosmic rays of rigidities 1.9 gv to 3 tv with the alpha magnetic spectrometer on the international space station. *Phys. Rev. Lett.*, 115, 211101.
10. Aguilar, M., Aisa, D., Alpat, B., Alvino, A., Ambrosi, G., Andeen, K., et al. (2015). Precision Measurement of the Proton Flux in Primary Cosmic Rays from Rigidity 1 GV to 1.8 TV with the Alpha Magnetic Spectrometer on the International Space Station. *Physical Review Letters*, 114(17), 171103.
11. Amsler, C., et al. (2008). Particle data group. *Phys. Lett. B*, 667(1).
12. Atwater, T. W., & Freier, P. S. (1986a). Meson multiplicity versus energy in relativistic nucleus-nucleus collisions. *Phys. Rev. Lett.*, 56, 1350–1353.
13. Atwater, T. W., & Freier, P. S. (1986b). Meson multiplicity versus energy in relativistic nucleus-nucleus collisions. *Physical review letters*, 56(13), 1350.
14. Atwood, W., Albert, A., Baldini, L., Tinivella, M., Bregeon, J., Pesce-Rollins, M., et al. (2013). Pass 8: Toward the Full Realization of the Fermi-LAT Scientific Potential. *arXiv e-prints*, arXiv:1303.3514.
15. Atwood, W. B., Abdo, A. A., Ackermann, M., Althouse, W., Anderson, B., Axelsson, M., et al. (2009). The Large Area Telescope on the Fermi Gamma-Ray Space Telescope Mission. *The Astrophysical Journal*, 697, 1071–1102.
16. Baldini, L. (2014). Space-based cosmic-ray and gamma-ray detectors: a review. *arXiv preprint arXiv:1407.7631*.
17. Becquerel, H. (1896). On the rays emitted by phosphorescence. *Compt. Rend. Hebd. Seances Acad. Sci.*, 122(8), 420–421.
18. Belolaptikov, I., Budnev, N., Sinegovsky, S., Padusenko, A., Wiebusch, C.,

Moroz, A., et al. (1997). The baikal underwater neutrino telescope: Design, performance and first results. Tech. rep., SCAN-9704016.

19. Beringer, J., Arguin, J. F., Barnett, R. M., Copic, K., Dahl, O., Groom, D. E., et al. (2012). Review of particle physics. *Phys. Rev. D*, 86, 010001.
20. Bird, D., Corbato, S., Dai, H., Dawson, B., Elbert, J., Emerson, B., et al. (1994). The cosmic-ray energy spectrum observed by the fly's eye. *The Astrophysical Journal*, 424, 491–502.
21. Carlson, A., Hooper, J., & King, D. (1950). Lxiii. nuclear transmutations produced by cosmic-ray particles of great energy.-*Part V.* the neutral mesons. *Philosophical Magazine Series 7*, 41(318), 701–724.
22. Clay, J. (1927). Penetrating Radiation I. In Proceedings of the Royal Academy of Sciences Amsterdam. vol. 30, pp. 1115–1127.
23. Clay, J. (1928). Penetrating Radiation II. In Proceedings of the Royal Academy of Sciences Amsterdam. vol. 31, pp. 1091–1097.
24. Compton, A. H., & Turner, R. (1937). Cosmic rays on the pacific ocean. *Physical Review*, 52(8), 799.
25. Curie, M. (1923). Pierre Curie. Macmillan.
26. De Angelis, A. (2014). Atmospheric ionization and cosmic rays: studies and measurements before 1912. *Astroparticle Physics*, 53, 19–26.
27. Dembinski, H. P., Engel, R., Fedynitch, A., Gaisser, T., Riehn, F., & Stanev, T. (2017). Data-driven model of the cosmic-ray flux and mass composition from 10 GeV to 10^{11} GeV. In Proceedings of 35th International Cosmic Ray Conference — PoS(ICRC2017). Sissa Medialab.
28. Dermer, C. D., & Powale, G. (2013). Gamma rays from cosmic rays in supernova remnants. *Astronomy & Astrophysics*, 553, A34.
29. Dorman, L. (2009). First measurements of cosmic ray geomagnetic effects and the problem of CR nature. In Astrophysics and Space Science Library, Springer Netherlands. pp. 1–8.
30. Dorman, L. I., Fedchenko, S. G., Granitsky, L. V., & Rishe, G. A. (1970). Coupling and barometer coefficients for measurements of cosmic ray variations at altitudes of 260-400 mb. In International Cosmic Ray

Conference. vol. 2, p. 233.

31. Ertley, C. (2014). Studying the polarization of hard x-ray solar flares with the gamma ray polarimeter experiment (grape).
32. Fermi, E. (1949). On the origin of the cosmic radiation. *Physical review*, 75(8), 1169.
33. Fricke, R. G., & Schlegel, K. (2017). Julius elster and hans geitel-dioscuri of physics and pioneer investigators in atmospheric electricity. *History of Geo-and Space Sciences*, 8(1), 1.
34. Gaisser, T. K., Stanev, T., & Tilav, S. (2013). Cosmic ray energy spectrum from measurements of air showers. *Frontiers of Physics*, 8(6), 748–758.
35. Gerward, L. (1999). Paul villard and his discovery of gamma rays. *Physics in perspective*, 1(4), 367–383.
36. Gray, G. W. (1949). Cosmic rays. *Scientific American*, 180(3), 28–39.
37. Greisen, K. (1966). End to the cosmic-ray spectrum? *Physical Review Letters*, 16(17), 748–750.
38. Haino, S., Sanuki, T., Abe, K., Anraku, K., Asaoka, Y., Fuke, H., et al. (2004). Measurements of primary and atmospheric cosmic-ray spectra with the bess-tev spectrometer. *Physics Letters B*, 594(1-2), 35–46.
39. Halzen, F., & Klein, S. R. (2010). Invited review article: Icecube: an instrument for neutrino astronomy. *Review of Scientific Instruments*, 81(8), 081101.
40. Hess, V. F. (1912). Über beobachtungen der durchdringenden strahlung bei sieben freiballonfahrten. *Phys. Z.*, 13, 1084–1091.
41. Huelsenbeck, J. P., & Crandall, K. A. (1997). Phylogeny estimation and hypothesis testing using maximum likelihood. *Annual Review of Ecology and Systematics*, 28(1), 437–466.
42. Hörandel, J. R. (2013). Early cosmic-ray work published in german. *AIP Conference Proceedings*, 1516(1), 52–60.
43. Isbert, J., Case, G., Granger, D., Guzik, T. G., Price, B., Stewart, M., et al. (2002). Atic, a Balloon Borne Calorimeter for Cosmic Ray Measurements. In CALORIMETRY IN PARTICLE PHYSICS. Proceedings of the Tenth International Conference. Held 25-29 March 2002 in Pasadena. pp. 89–94.

44. Kachelrieß, M., & Ostapchenko, S. (2012). Deriving the cosmic ray spectrum from gamma-ray observations. *Phys. Rev. D*, 86, 043004.

45. Kelner, S. R., Aharonian, F. A., & Bugayov, V. V. (2006). Energy spectra of gamma rays, electrons, and neutrinos produced at proton-proton interactions in the very high energy regime. *Physical Review D*, 74(3), 034018.

46. Kennedy, J., & Eberhart, R. (1995). Particle swarm optimization. In Proc. of ICNN'95 - Int. Conf. on Neural Networks. Perth, WA, Australia, vol. 4, p. 1942.

47. Kirk, T. B., & Neddermeyer, S. H. (1968). Scattering of high-energy positive and negative muons on electrons. *Physical Review*, 171(5), 1412.

48. Kolhörster, W. (1934). Cosmic rays under 600 metres of water. *Nature*, 133(3359), 419–419.

49. Kraushaar, W., & Clark, G. (1962). Search for primary cosmic gamma rays with the satellite explorer xi. *Physical Review Letters*, 8(3), 106.

50. Kraushaar, W., Clark, G., Garmire, G., Helmken, H., Higbie, P., & Agogino, M. (1965). Explorer xi experiment on cosmic gamma rays. *The Astrophysical Journal*, 141, 845.

51. Kraushaar, W. L., Clark, G. W., Garmire, G. P., Borken, R., Higbie, P., Leong, V., & Thorsos, T. (1972). High-Energy Cosmic Gamma-Ray Observations from the OSO-3 Satellite. *The Astrophysical Journal*, 177, 341.

52. Lesur, V. (2006). Introducing localized constraints in global geomagnetic field modelling. *Earth, planets and space*, 58(4), 477–483.

53. Linsley, J. (1963). Evidence for a primary cosmic-ray particle with energy 10 20 ev. *Physical Review Letters*, 10(4), 146.

54. Madlee, S., Mitthumsiri, W., Ruffolo, D., Digel, S., & Nuntiyakul, W. (2020). First analysis of earth's stratospheric gamma-ray emission in geographical coordinates with fermi lat. *Journal of Geophysical Research: Space Physics*, 125, 28151.

55. Maldera, S. (2019). Fermi-lat performance,. `https://www.slac.stanford.`

edu/exp/glast/groups/canda/lat_Performance.htm. Accessed: 2021-04-19.

56. Michelson, P. F., Atwood, W. B., & Ritz, S. (2010). Fermi gamma-ray space telescope: high-energy results from the first year. *Reports on Progress in Physics*, 73(7), 074901.
57. Millikan, R. A. (1932). Cosmic-ray ionization and electroscope-constants as a function of pressure. *Physical Review*, 39(3), 397.
58. M.J. Berger, J. H. (2010). Xcom: Photon cross sections database. (accessed: 07.06.2018).
59. Morris, D. J. (1984). Production of high-energy gamma rays by cosmic ray interactions in the atmosphere and lunar surface. *Journal of Geophysical Research*, 89, 10685–10696.
60. Morrison, P. (1958). On gamma-ray astronomy. *Il Nuovo Cimento (1955-1965)*, 7(6), 858–865.
61. Neddermeyer, S. H., & Anderson, C. D. (1937). Note on the nature of cosmic-ray particles. *Physical Review*, 51(10), 884.
62. Nuntiyakul, W., Evenson, P., Ruffolo, D., Sáiz, A., Bieber, J. W., Clem, J., et al. (2014). Latitude Survey Investigation of Galactic Cosmic Ray Solar Modulation during 1994-2007. *The Astrophysical Journal*, 795, 11.
63. Orth, C. D., & Buffington, A. (1976). Secondary cosmic-ray electrons and positrons from 1 to 100 gev in the upper atmosphere and interstellar space, and interpretation of a recent positron flux measurement. *The Astrophysical Journal*, 206, 312–332.
64. Petry, D. (2005). The Earth's Gamma-ray Albedo as observed by EGRET. In F. A. Aharonian, H. J. Völk, & D. Horns (Eds.), High Energy Gamma-Ray Astronomy. *American Institute of Physics Conference Series*, vol. 745, pp. 709–714.
65. Rochester, G., & Butler, C. (1953). The new unstable cosmic-ray particles. *Reports on Progress in Physics*, 16(1), 364.
66. Rossi, B. (1930). On the Magnetic Deflection of Cosmic Rays. *Physical Review*, 36, 606–606.

67. Rossi, B. (1934). Directional measurements on the cosmic rays near the geomagnetic equator. *Phys. Rev.*, 45, 212–214.

68. Rossi, B., & Greisen, K. (1941). Cosmic-ray theory. *Reviews of Modern Physics*, 13(4), 240.

69. Ruffolo, D., Sáiz, A., Mangeard, P.-S., Kamyan, N., Muangha, P., Nutaro, T., et al. (2016). Monitoring Short-term Cosmic-ray Spectral Variations Using Neutron Monitor Time-delay Measurements. *The Astrophysical Journal*, 817, 38.

70. Seo, E., Ahn, H., Beatty, J., Coutu, S., Choi, M., DuVernois, M., et al. (2004). Cosmic-ray energetics and mass (cream) balloon project. *Advances in Space Research*, 33(10), 1777–1785. The Next Generation in Scientific Ballooning.

71. Shea, M., Smart, D., & McCracken, K. (1965). A study of vertical cutoff rigidities using sixth degree simulations of the geomagnetic field. *Journal of Geophysical Research*, 70(17), 4117–4130.

72. Sigl, G. (2012). High energy neutrinos and cosmic rays. *arXiv preprint arXiv:1202.0466*.

73. Skobeltzyn, D. (1929). The Angular Distribution of Compton Recoil Electrons. *Nature*, 123(3098), 411–412.

74. Skobeltzyn, D. V. (1985). The early stage of cosmic ray particle research. In Early History of Cosmic Ray Studies, Springer. pp. 47–52.

75. Stecker, F. W. (1973). Simple Model for Scanning-angle Distribution of Planetary Albedo Gamma-rays. *Nature Physical Science*, 242, 59–60.

76. Stephens, S. A., & Badhwar, G. D. (1981). Production spectrum of gamma rays in interstellar space through neutral pion decay. *Astrophysics and Space Science*, 76, 213–233.

77. Störmer, C. (1934). Critical remarks on a paper by g. lemaître and ms vallarta on cosmic radiation. *Physical Review*, 45(11), 835.

78. Svensson, G. (1958). The cosmic ray photon and π^0-meson energy spectra at 29-30 km above sea-level. *Arkiv Fysik*, 13, 347.

79. Taylor, A. M. (2016). Cosmic rays beyond the knees. *Nature*, 531(7592), 43–44.

80. Thébault, E., Finlay, C. C., Beggan, C. D., Alken, P., Aubert, J., Barrois, O., et al. (2015). International geomagnetic reference field: the 12th generation. *Earth, Planets and Space*, 67(1), 79.

81. Thompson, D. J., Simpson, G. A., & Ozel, M. E. (1981). SAS 2 observations of the earth albedo gamma radiation above 35 MeV. *Journal of Geophysical Research*, 86, 1265–1270.

82. Trenn, T. J. (1976). Rutherford on the alpha-beta-gamma classification of radioactive rays. *Isis*, 67(1), 61–75.

83. Tsyganenko, N. A. (1987). Global quantitative models of the geomagnetic field in the cislunar magnetosphere for different disturbance levels. *Planetary and Space Science*, 35, 1347–1358.

84. Ütikofer, R. B. (2007). 30th international cosmic ray conference characteristics of near real-time cutoff calculations on a local and global scale.

85. Van Allen, J. A., & Frank, L. A. (1959). Radiation around the earth to a radial distance of 107,400 km. *Nature*, 183(4659), 430–434.

86. Van Oosterom, A., & Strackee, J. (1983). The solid angle of a plane triangle. *IEEE Transactions on Biomedical Engineering*, BME-30(2), 125–126.

87. Wallace, J. M., & Hobbs, P. V. (2006). Atmospheric. Science.

88. Watson, A. (2000). Ultra-high-energy cosmic rays: the experimental situation. *Physics Reports*, 333, 309–327.

89. Wilks, S. S. (1938). The large-sample distribution of the likelihood ratio for testing composite hypotheses. *Ann. Math. Statist.*, 9(1), 60–62.

90. Wilson, C. T. R. (1921). Iii. investigations on lighting discharges and on the electric field of thunderstorms. *Philosophical Transactions of the Royal Society of London. Series A, Containing Papers of a Mathematical or Physical Character*, 221(582-593), 73–115.

91. Yoshida, S., Hayashida, N., Honda, K., Honda, M., Imaizumi, S., Inoue, N., et al. (1994). Lateral distribution of charged particles in giant air showers above 1 eev observed by agasa. *Journal of Physics G: Nuclear and Particle Physics*, 20(4), 651.

APPENDICES

APPENDIX A
PARALLEL COMPUTATION OF THE EXPOSURE MAP

Long calculation time for the exposure calculation comes from two matrix transformations to accumulate the LAT exposure when the Earth is in the FoV.

For each step time, the transformation matrix is calculated from the information of spacecraft orientation. After that, each nadir angle represented in equatorial coordinates (Equation 4.2.1) is transformed into angles in the plane of detector (Equation 4.6). Hence, we can calculate the exposure for a given nadir angle by summing the LAT exposure time multiplied with the effective area for the corresponding incidence angle and energy.

The resolution of the exposure map impacts the computational time. Assuming that there are M bins in θ_{NADIR} axis and N bins in ϕ_{NADIR} axis. It costs $\mathcal{O}(MN)$ multiplied by the complexity of two transformation matrices to compute a single exposure map. This complexity will be multiplied by 50 times since we have 50 energy bins.

The first version of Python code takes around 1435 seconds to finish one week of FT2 data. In addition, the matrix transformation already uses Numpy for all matrix operations which means that the plain Python code likely to takes longer than this speed. In the meantime, using serial a serial C++ code takes around 12 seconds to finish the workload of 1-week data, showing ~ 120 times faster for the compiling language.

The parallel code is implemented in the C++ programming language with Message Passing Interface (MPI). We use Master-Slave techniques to fully utilize the CPU resources where the master process is monitoring and sending tasks to all workers. Only one master process is needed to allow the program to scale

horizontally (multi-node scaling) by adjusting the number of slave processes.

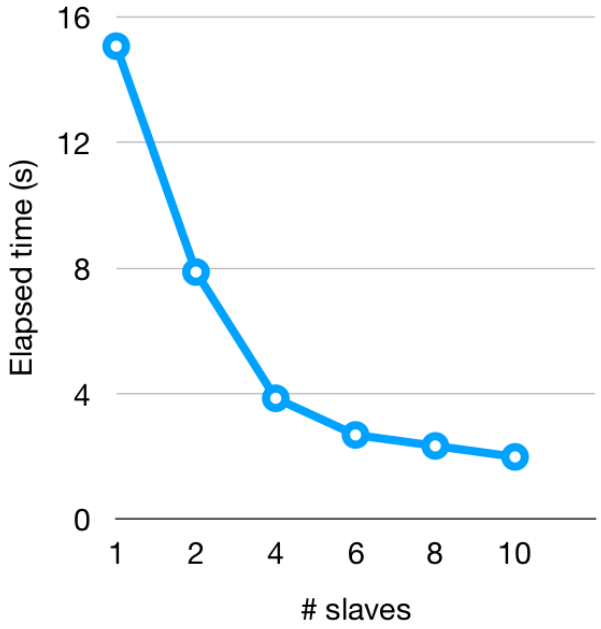

Figure A.1: Benchmarking of the serial and parallel code in the low level language.

The hardware used to benchmark is composed of 6 cores and 12 threads. Figure A.1 shows the scalability of the code in terms of the elapsed time which is exponentiall decreasing with the number of slave processes. The plateau curve on the edge is from the fact that the maximum available running threads on this hardware are only twelve which means that more workers that exceeds this limit do not reduce the computation time. However, the total CPU cores on the cluster in space physics laboratory are around 200 thread executors. The performance from running the parallel code in the cluster takes only about twelve hours to finish.

APPENDIX B
POWER LAW IN ENERGY

Equation 4.7 and Equation 4.8 express the spectral power law in rigidity. We can derive them into the energy spectrum as in Equation B.1 and Equation B.2 respectively.

Single power law (SPL)

The energy spectrum in energy is derived as

$$\frac{dN}{dE} = N_0[E_k(E_k + 2m_p)]^{-\gamma/2} \left(\frac{E_k + m_p}{\sqrt{E_k(E_k + 2m_p)}} \right) \tag{B.1}$$

where m_p is the mass of proton and E_k is the kinetic energy and N_0 is defined as the normalization factor.

Broken power law (BPL)

$$\frac{dN}{dE} = \begin{cases} N_0[E_k(E_k + 2m_p)]^{-\gamma_1/2} \left(\frac{E_k+m_p}{\sqrt{E_k(E_k+2m_p)}} \right) & : \ E < E_{\text{Break}} \\ N_0[E_b(E_b + 2m_p)]^{(\gamma_2-\gamma_1)/2}[E_k(E_k + 2m_p)]^{-\gamma_2/2} \left(\frac{E_k+m_p}{\sqrt{E_k(E_k+2m_p)}} \right) & \\ : \ E \geq E_{\text{Break}} & \end{cases} \tag{B.2}$$

where the symbols are defined in the same way as Equation B.1.

APPENDIX C
SUBTRACTING γ-RAY BACKGROUND

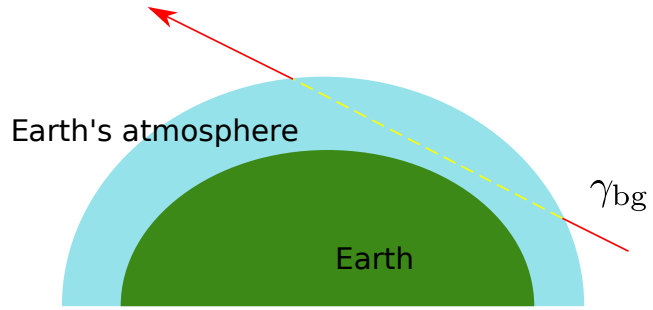

Figure C.1: Schematics of γ-ray propagation from diffusive background

Assuming the classical collision process, we obtain

$$N \equiv N_0 e^{-n\sigma x} \tag{C.1}$$

when

- N is the surviving number of photons
- N_0 is the original number of photons
- n is a density of the air
- σ is a crossection of the γ-ray and the air
- x is a propagation length.

From using cross-section data from M.J. Berger (2010), we find that collision probability of a γ-ray with a nitrogen atom and that with an oxygen atom are similar in the energy range of our interest. If we consider a worst-case scenario

(longest path and highest density that could happen in the upper atmosphere of our interest), we find that the possibility of a diffuse background photon passing through approaches one. Therefore, we can straightforwardly remove the background contamination by using an estimation from the average sky diffusive intensity.

APPENDIX D
INTERACTION MODEL

Since we are regarding the proton interaction with the Earth's atmosphere as thin-target proton-proton interaction regime. We can calculate the γ-ray spectrum from the incident proton spectrum colliding with nitrogen atoms as

$$\frac{dN_\gamma}{dE_\gamma} \propto \int_{E_\gamma}^{E_{\max}} dE' \frac{dN_p}{dE'} \frac{d\sigma^{pp\to\gamma}(E', E_\gamma)}{dE_\gamma}. \tag{D.1}$$

This equation can be changed to a discrete form as

$$\frac{dN_\gamma}{dE_\gamma} \propto \sum_{E'=E_\gamma}^{E_{\max}} \frac{E'}{E_\gamma} \Delta(\ln E') E_\gamma \frac{d\sigma^{pp\to\gamma}}{dE_\gamma} \frac{dN_p}{dE'}. \tag{D.2}$$

We can add the contribution from α particles and define $f_{pp} \equiv E_\gamma (d\sigma^{pp\to\gamma}/dE_\gamma)$ from the K&O model (Kachelrieß & Ostapchenko 2012) to obtain

$$\begin{aligned} \frac{dN_\gamma}{dE_\gamma} &\propto \sum_{E'=E_\gamma}^{E_{\max}} \frac{E'}{E_\gamma} \Delta(\ln E') \left[E_\gamma \frac{d\sigma^{pN\to\gamma}}{dE_\gamma} \left(\frac{dN_p}{dE'} \right) + E_\gamma \frac{d\sigma^{\alpha N\to\gamma}}{dE_\gamma} \left(\frac{dN_\alpha}{dE'} \right) \right] \\ &\propto \sum_{E_i'} \left[\frac{E_i'}{E_\gamma} \Delta(\ln E_i') \right] \left[f_{pp} \frac{dN_p}{dE_i'} \left\{ 1 + \frac{\sigma_{\alpha\mathrm{N}}}{\sigma_{p\mathrm{N}}} \left(\frac{dN_p}{dR} \right)^{-1} \frac{dN_\alpha}{dR} \frac{dR_\alpha}{dR_p} \right\} \right] \end{aligned} \tag{D.3}$$

Here we use the ratio of α-nitrogen to proton-nitrogen cross section from the parametrization by Atwater & Freier (1986a) and find $\sigma_{\mathrm{HeN}}/\sigma_{\mathrm{pN}} \approx 1.77$. We also use $dR_\alpha/dR_p \approx 2$ at the same energy in the relativistic limit.

APPENDIX E
MONTE CARLO SIMULATION

The error of the optimized results can be estimated from Monte Carlo simulation for both statistical deviation as well as taking the systematical error from the apparatus into account as the total error.

Since the complexity in the heuristic optimizations much higher than the plain gradient descent method. In this simulation for estimating the deviation, the optimization process is conducted from applying the gradient descent method with a given global optimized results. The distribution outcome of each parameter will be fitted for finding the deviation via normal distribution function. The mean value of the function will be fixed by the best global optimization.

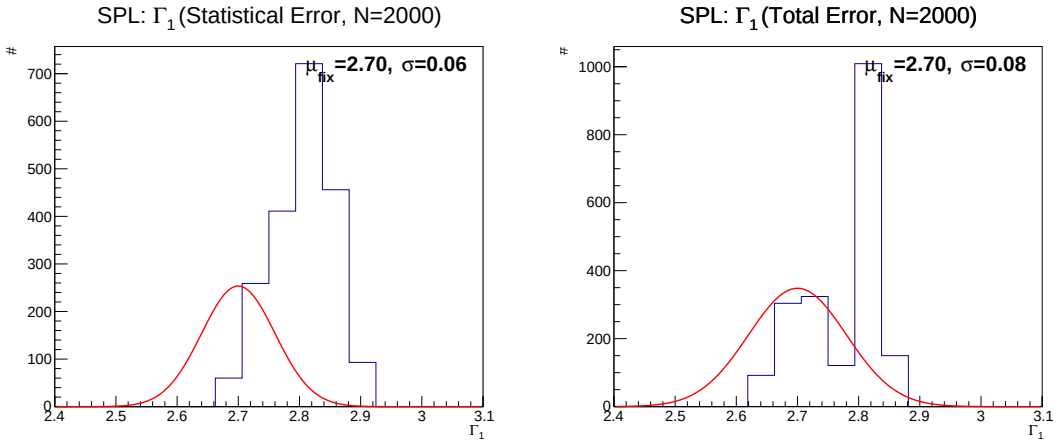

(a) Statistical deviation (b) Total deviation

Figure E.1: The distribution of the fitted results by SPL model from the distortion.

Simulation process for statistical deviation is done by rescaling the spectrum from the information of the arrival photon. The discrete probability of the events from a fixed amount of time could be modeled by using poisson distribution function. Hence, the photon spectrum in each energy bin will be rescaled by resampling photon numbers from a given amount of photon from

observations as the number of occurrences.

The results from the statistical simulation for SPL is shown in Figure E.1a as well as Figure E.2 demonstrates the deviation of BPL model.

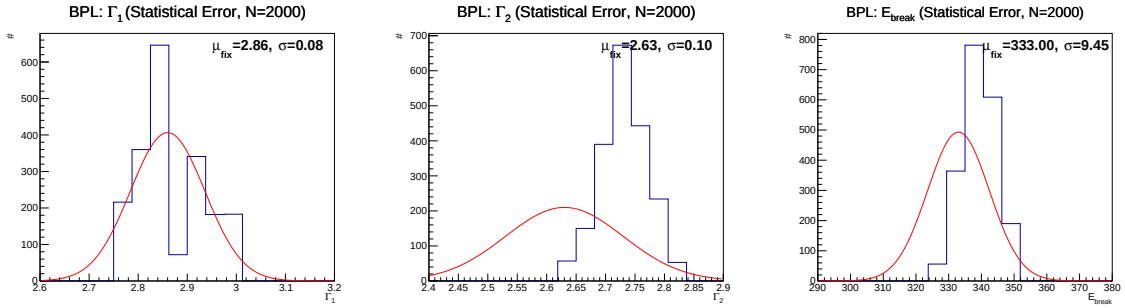

(a) First spectral index (b) Second spectral index (c) Breaking energy

Figure E.2: Statistical simulation of the BPL model

On the other hand, total deviation is taken the systematical distortion into account. It is modeled as an uncertain from the detector[1]. First step for generating spectrum is exactly the same as the statistical error. The following step is to purturb the spectrum by the distorted curved. The curved is computed by sample three different points in 3 energy decades (10 GeV, 100 GeV and 1 TeV).

The results of the total error of SPL model is illustrated in Figure E.1b and the deviation of the BPL parameters is shown in Figure E.3.

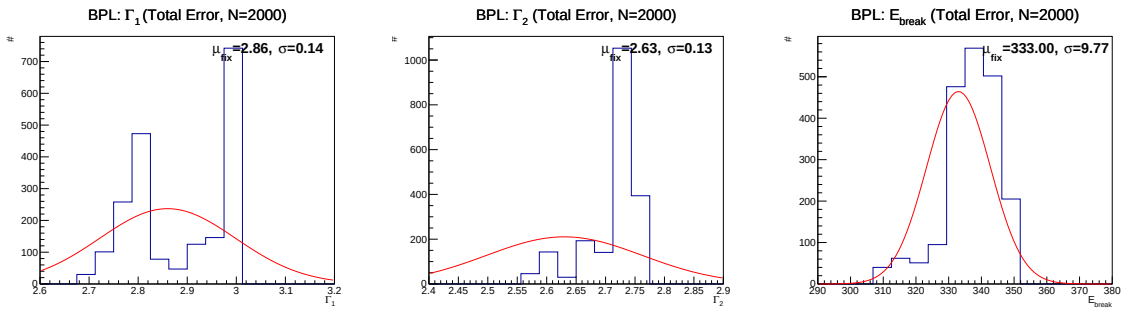

(a) First spectral index (b) Second spectral index (c) Breaking energy

Figure E.3: Statistical and systematical (Total) simulation of the BPL model

[1] https://fermi.gsfc.nasa.gov/ssc/data/analysis/scitools/Aeff_Systematics.html

APPENDIX F
ANALYSIS OF γ-RAY FROM NORTH AND SOUTH DIRECTIONS

According to photon intensity in Earth's centered coordinates shows the higher density in the North-South direction comparing the East-West direction (Figure 5.7). The clue might come from exposure time in the North and South direction is much higher than the east and west in Figure 5.5. Performing an analysis of the North-South's γ-ray spectrum to compare with the full limb's photon could be a good option for investigating the quality of the analysis.

The North-South spectrum is obtained by applying condition of $\phi_{\mathrm{NADIR}} \in (-30^{\circ}, 30^{\circ})$ for collecting spectrum from the North and the $\phi_{\mathrm{NADIR}} \in (150^{\circ}, 210^{\circ})$ for accumulating the spectrum from the South. The γ-ray spectrum is plotted in Figure F.1 on par with the optimization results from both SPL and BPL models.

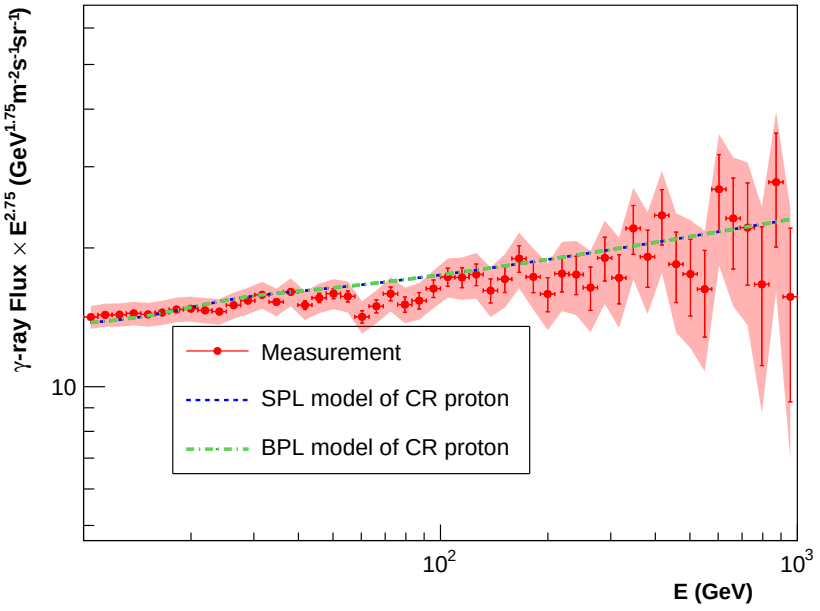

Figure F.1: North-South limb's γ-ray spectrum and the fitted models.

Table F.1 shows the fitted parameters from particle swarm optimization and the scaled results of modeled proton spectrum is visualized in Figure F.2. According to Table 5.1, the outcome from this analysis shows the consistency where it aligns within 1σ of the deviation.

Best fits	Γ_1	Γ_2	E_{Break} (GeV)
SPL	2.63	-	-
BPL	2.90	2.65	327

Table F.1: Optimization results from the North-South spectrum.

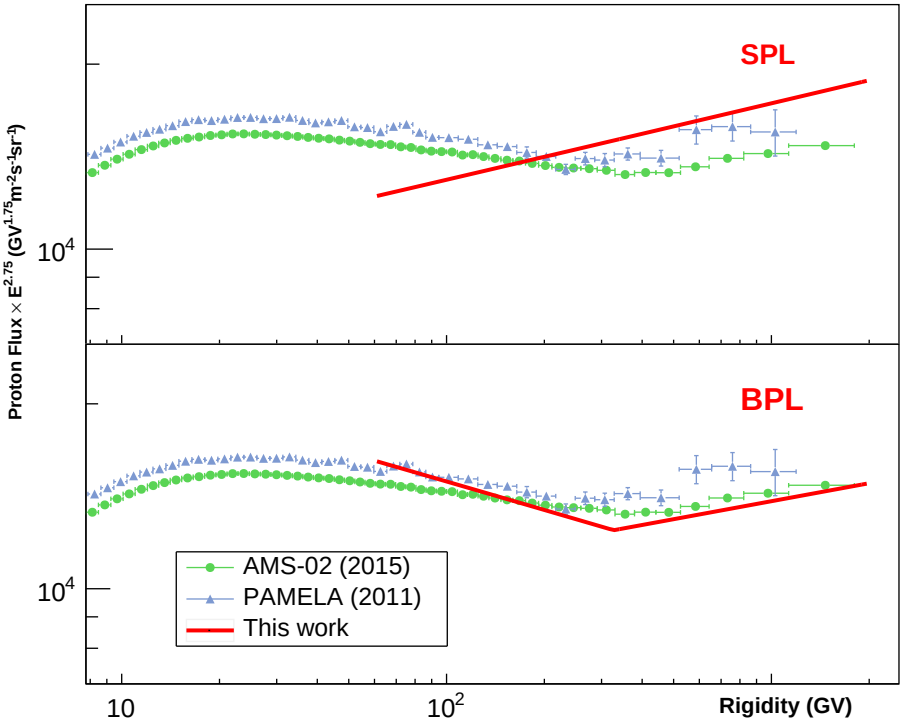

Figure F.2: Best-fit CR proton spectrum from North-South γ-ray spectrum (red) compared to the measurements by AMS-02 (blue) and PAMELA (green).

APPENDIX G
EFFECTIVE AREA OF ULTRACLEANVETO

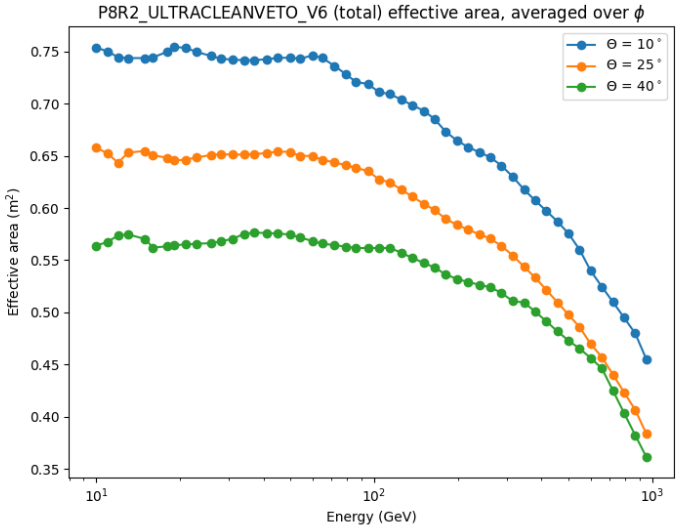

Figure G.1: Effective area versus photon energy

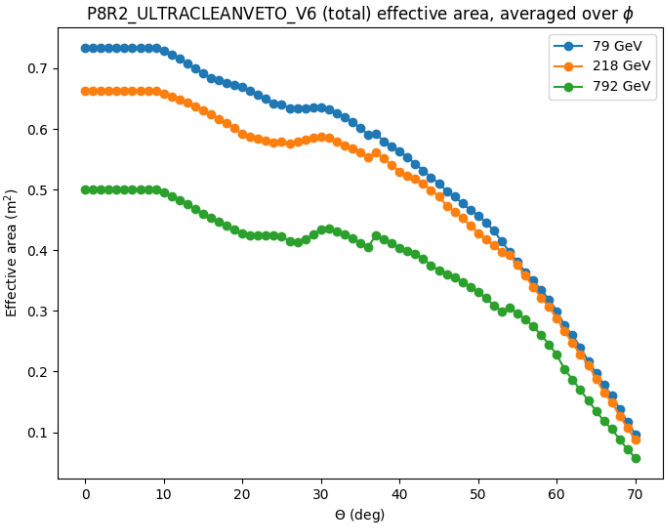

Figure G.2: Effective area versus incident angle

BIOGRAPHY

NAME	Mr. Patomporn Payoungkhamdee
DATE OF BIRTH	29 April 1996
PLACE OF BIRTH	Bangkok, Thailand
INSTITUTIONS ATTENDED	Mahidol University, 2014–2017 Bachelor of Science (Physics) Mahidol University, 2018–2020 Master of Science (Physics)
HOME ADDRESS	86/46 Moo. 7, Bangmuang, Muang, Samutprakan 10270 Thailand
E-MAIL	patomporn.pay@student.mahidol.ac.th